Design and Characterization of Harmonic Rotor Thrust Vector Control for Micro Aerial Vehicles

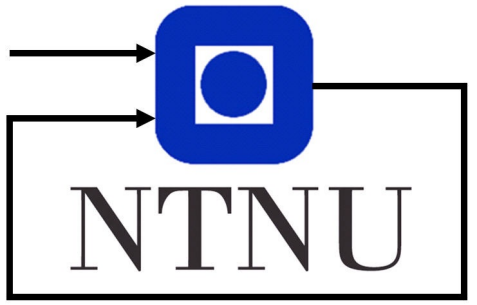

Author:
Håvard Brenne

Supervisor:
Prof. Dr. Kostas Alexis

Specialization project
Department of Engineering Cybernetics
Norwegian University of Science and Technology

December 19, 2022

Acknowledgements

I would like to express my gratitude to my supervisor Professor Kostas Alexis, and advisor Ph.D. candidate Paolo De Petris for the guidance, support, and encouragement throughout the duration of this project. I am thankful for the opportunity to work on such an exciting project and for the resources provided to me to implement it. I am also grateful for the help gotten from members of the Autonomous Robots Lab at NTNU throughout the project. I would like to specifically thank Ph.D. candidate Jørgen Anker Olsen for assistance with experiment implementation.

Abstract

Micro aerial vehicles typically use rigid propellers with a static thrust vector direction. In the case of a traditional helicopter rotor, thrust vectoring can be performed using two additional actuators and a complex swashplate. Thrust vector control of a rotor without a swashplate is experimentally shown in this project by harmonically controlling a single actuator. The control relies on specific passive rotor hinges that allows kinematic coupling to be exploited for control in the underactuated system. Controlling a thrust vector can achieve new benefits in control, reduction of actuators and efficiency. Such a rotor design has been developed and implemented. The design of the thrust controlled rotor builds upon previous work on this mechanism, with an expansion to high performance motor control with a field oriented control method. Compared to previous work, the harmonic modulation is proposed in terms of mechanical rather than electrical output, and can be directly applied with torque control.

Table of Contents

List of Tables

List of Figures

Abbreviations

Abbreviation	Description
MAV	Micro Aerial Vehicle
BEMT	Blade element momentum theory
FOC	Field oriented control
PMSM	Permanent magnet synchronous motor
BLDCM	Brushless direct current motor
PWM	Pulse width modulation
EMF	Electromotive force
PI-controller	Proportional integral controller
CAN-FD	Controller area network flexible data-rate
IMU	Inertial measurement unit

1

Introduction

The quadcopter configuration is by far the most common micro aerial vehicle (MAV) configuration in use, both in industry and research. The simple mechanical design of only four moving parts is advantageous, especially compared to configurations such as the traditional helicopter with a mechanically complex swashplate mechanism. As MAVs are often low-cost, high volume and used in less controlled environments than the helicopter, the low maintenance and cost of the simple mechanical design is crucial. Other MAV configurations can offer advantages over the quadcopter, especially for specific applications. Adapting a cyclical pitch controllable rotor such as in the helicopter enables configurations with fewer, and comparatively larger propellers than that of the quadcopter. Designing a miniaturized swashplate mechanism is difficult. It requires two extra actuators to control the blade pitch, in addition to miniaturized coupling and swashplate mechanism. This increases the mechanical complexity substantially, as well as the cost, weight and

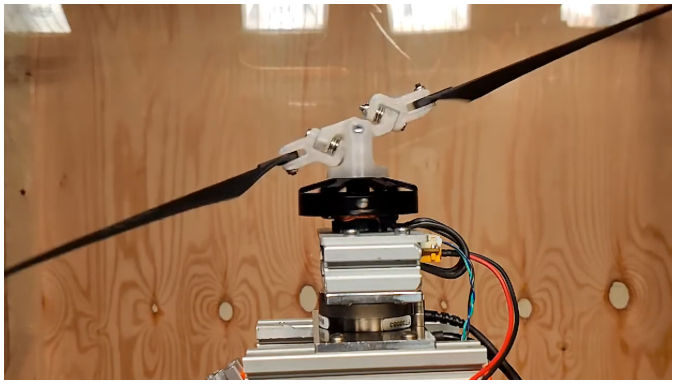

Figure 1.1: Still frame from high frame rate video of thrust vectored rotor by harmonic motor control. A demonstration of the implemented design can be found at `https://youtu.be/ZwSBDbz_Pnw`

maintenance requirements. The total number of actuators will still amount to four for a conventional helicopter, one main motor, a tail rotor and two actuators to control collective and cyclical pitch of the main rotor.

An alternative mechanism exists for cyclical pitch control. Rather than using a mechanical swashplate with additional actuators, the blade pitch is cyclically controlled by the main motor. A specific hinged rotor articulation enables once-per-revolution harmonic motor torque modulation to induce a rotor pitch angle. It is an underactuated system with no additional actuators or swashplate required. The main concept consists of kinematically coupling blade lag and blade pitch through a skewed lag-pitch hinge. Acceleration of the motor causes blade lag, which couples to blade pitch. Having a positive lag-pitch coupling on one blade, and a negative lag-pitch coupling on the opposite blade, allows a blade pitch difference. A desired blade pitch difference at positions within a rotation can be controlled by harmonically modulating motor torque.

Having a cyclical pitch control mechanism suitable for MAVs can potentially have several advantages. For a helicopter MAV configuration, one needs only two actuators instead of four, in addition to a simpler mechanical system. Other configurations that could benefit include the bi-copter and coaxial MAV. Bi-copters, with two main rotors in the same plane, have typically used servo motors to tilt the rotors and achieve control. These servo motors could be replaced by the mentioned pitch control technique. Additionally, the servo controlled bi-copter has been shown to have the inherent undesired property of non-minimum phase roll dynamics (Li et al. (2020)), fundamentally limiting controller bandwidth. The physical explanation given of this phenomenon is that the servo motor torque applied to tilt the whole rotor assembly causes an undesired moment in the opposite direction of desired motion, regardless of the control method used. This undesired moment is eliminated by only inducing cyclical pitch. Other MAV configurations could also benefit from cyclical pitch control. Most configurations have all actuators in the same plane, such that a force can only be applied in one direction, and it can therefore only linearly accelerate in this direction. With rotor pitch control, decoupling force from orientation could be achieved.

Usage of a swashplate-less cyclical pitch mechanisms in industry has been demonstrated by companies such as Flybotix and Vertiq. Flybotix claim their miniature, enclosed, coaxial MAV, enabled by swashplate-less cyclical pitch control, achieves twice the flight time of similar indoor drones (Flybotix (2022)). Vertiq has demonstrated swashplate-less pitch control as a technology demonstration (Vertiq (2022)).

For this alternative cyclical pitch method, accurate and high performance dynamic motor control is important. Additionally, the motor position needs to be either measured or estimated. Field oriented control (FOC) is a control technique used in electrical motors that has been a significant development in the field of motion control. The technique, which was developed in the 1970s, allows for precise and efficient control of an electrical motor's speed and torque, as well as improved energy efficiency. These advantages have made field oriented control a valuable tool in many industries, however it has not been the standard in most MAVs in industry and research.

1.1 Related work

The swashplate-less cyclical pitch concept has been studied previously. Paulos and Yim (2018) derived a dynamical model and performed experimental investigation of rotors articulated with one flap hinge, and one skewed lag-pitch hinge per blade. The flap hinge allows each blade to independently move up and down, relieving bending moments in the blade. It was shown to reduce stresses and vibrations compared to only using a skewed lag-pitch hinge. With only a skewed lag-pitch hinge, the blade pitch difference is transfered as moments in the rotor hub. With the addition of a flapping hinge, the blades can move up and down, tilting the blade tip path plane. The thrust vector is therefore controlled in addition to induced moments in the rotor hub. Paulos et al. (2018) combined the per-blade flap hinges into a central teetering hinge. This eliminates the moment transfers through the rotor hub, and enables control of the thrust vector. With this setup, a coaxial MAV configuration with two articulated rotors were shown to have actuation of forces and torques in 6 degrees of freedom. Qin et al. (2022) implemented the single teetering hinge configuration in a bi-copter design. The pin hinges used by previous work were exchanged by low friction radial and axial bearings. This eliminates non-linearities in friction at low drive amplitudes apparent in the rotor of Paulos and Yim (2018). Feasibility of a bi-copter with thrust vector control were experimentally shown, being able to track roll and pitch commands under disturbances, carrying a payload.

The dynamical model derived by Paulos and Yim (2018) builds on research on rotor aircraft. Orthogonal hinge angle parameterization is purposefully implemented to use previous results from modeling of helicopter rotors. A lag-pitch coupled hinge configuration for a rotor has been modeled by Bousman et al. (1990), where the use case of stability was studied, but it was not exploited for control. Paulos and Yim (2018) expands upon this model. Previous work such as rotor blade flap-lag modeling from Ormiston and Hodges (1972) is also used.

Field oriented control was developed in the 1970s. At this time, brushed DC motors were used for dynamical motor control, as AC induction motors were typically only possible to drive at a single speed. Elaschke and Böhm (1974) and Hasse (1969) developed methods to obtain the rotor flux vector, which was essential to control a AC motor similarly to a DC motor. The calculations needed for these methods requires significant computing power, and it has therefore seen a boost with embedded, low cost computing power. Bosso et al. (2021) investigated FOC for MAV propulsion system. Performance analysis both in simulations and experiments provides insight in the usage of FOC for MAVs.

1.2 Rotor thrust vector control concept

The thrust vector control concept to be studied in this project derives from the design of Qin et al. (2022), building on the design of Paulos and Yim (2018). This section contains a more intuitive overview of how the thrust vector control works.

Figure 1.2 shows the rotor, consisting of a motor, 2 blades, a central teetering hinge and two skewed lag-pitch hinges. The orientation of the skewed lag-pitch hinges is such that the blade marked as ”positive” obtains a positive coupling between blade lag and blade pitch, while the blade marked ”negative” obtains a negative coupling between blade lag

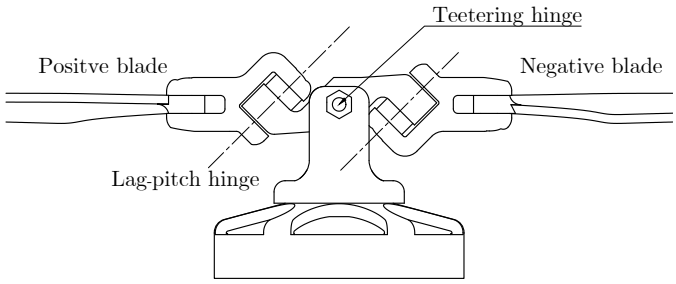

Figure 1.2: Rotor overview

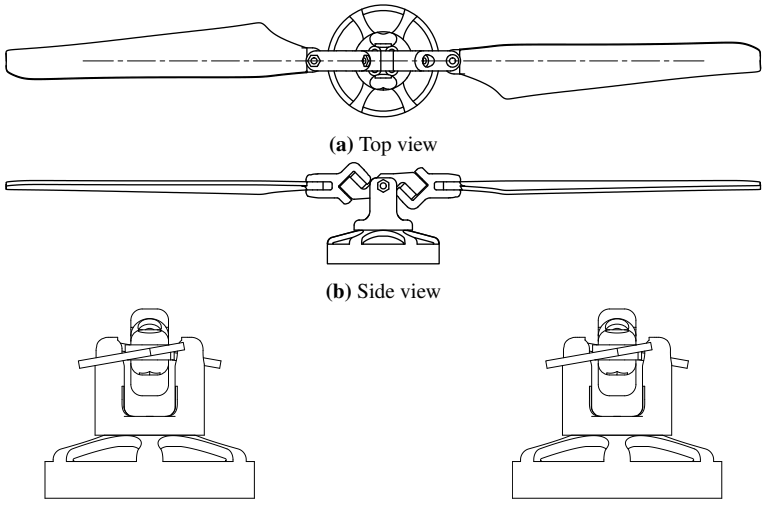

(a) Top view

(b) Side view

(c) Front view with positive lag-pitch coupling blade **(d)** Back view with negative lag-pitch coupling blade

Figure 1.3: Overview of rotor configuration with hinge angles equal zero. This corresponds to a conventional rotor configuration without hinges

and blade pitch. To illustrate the concept, a simplified thrust vector control sequence is presented.

Step 1: For simplicity, Figure 1.3 shows the rotor with hinge angles equal to zero, under the assumption that this is an equilibrium when spinning at a constant speed.

Step 2: The motor accelerates counter clockwise in Figure 1.4, causing both blades to lag behind the motor position due to their moment of inertia. This lag can be seen in Figure 1.4(a). As blade lag couples to blade pitch, a resulting increased blade pitch can be seen for the positive blade in Figure 1.4(c) and the corresponding left blade in Figure 1.4(b). A decreased blade pitch can be seen for the negative blade in Figure 1.4(d) and the corresponding right blade in Figure 1.4(b).

Step 3: The aerodynamic lift is proportional to the blade pitch, such that the thrust generated by the positive blade increases, and opposite for the negative blade. As the

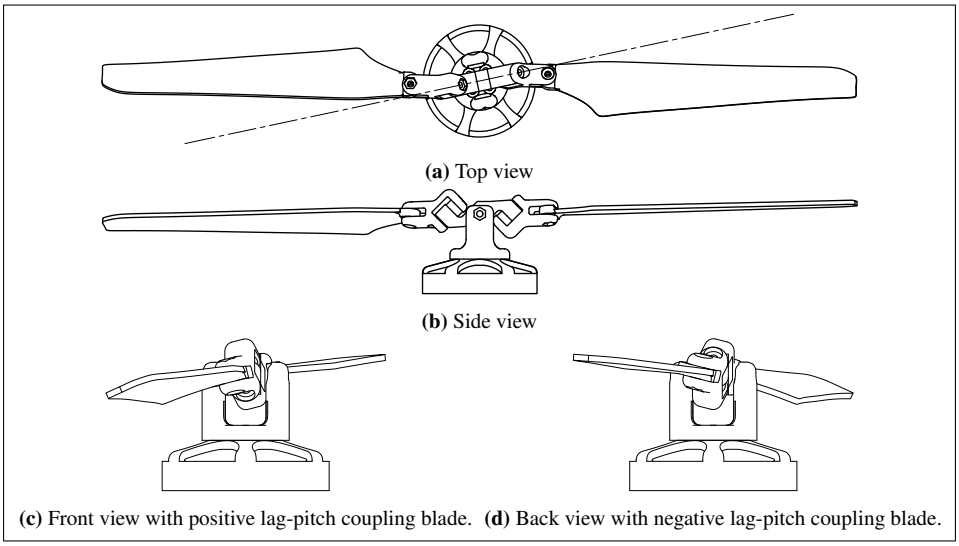

(a) Top view

(b) Side view

(c) Front view with positive lag-pitch coupling blade. **(d)** Back view with negative lag-pitch coupling blade.

Figure 1.4: Overview of rotor configuration with counter clockwise motor acceleration. The moment of inertia of the blades causes them to lag behind with a lag-pitch hinge angle. The positive blade obtains a higher pitch, while the negative blade obtains a lower pitch

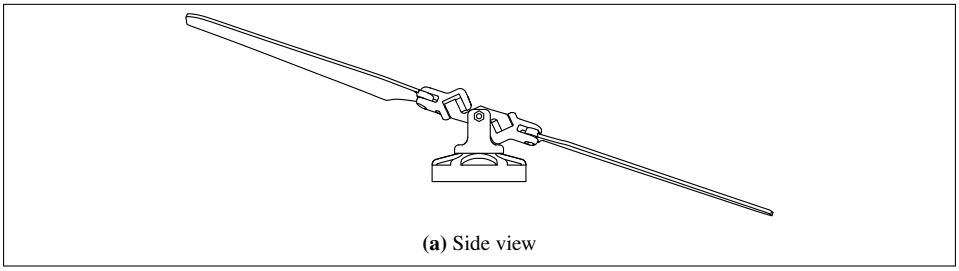

(a) Side view

Figure 1.5: Side view of rotor configuration with tilted thrust vector. Difference in blade pitch causes a difference in aerodynamic force between the blades. The side hub assembly rotates along the teetering hub, tilting the thrust disk.

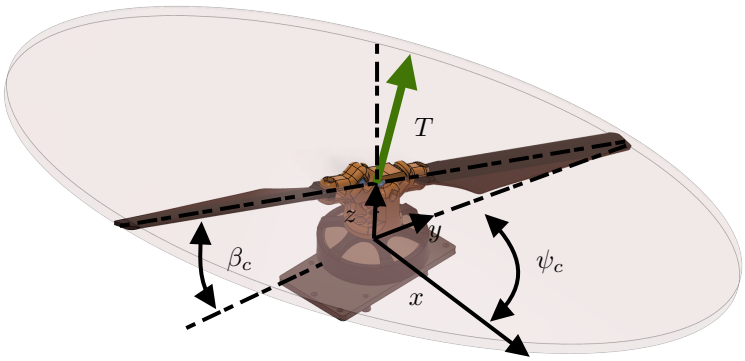

Figure 1.6: Propulsion disk and thrust vector. In this specific case the rotor is aligned with the azimuth angle ψ_c of maximum blade tip path plane angle β_c

blades can freely rotate about the teetering hinge, this difference in thrust causes the blades to tilt around the teetering hinge, seen in Figure 1.5.

Let Figure 1.5 illustrate the maximum teetering angle. To control a constant thrust vector direction, the teetering angle needs to follow a sinusoidal trajectory with respect to motor position. By decelerating the motor, the blades will lead the motor position due to their moment of inertia. Thus the opposite action to what was explained previously occurs, the positive blade pitch decreases, while the negative blade pitch increases.

1.3 Problem statement

The main objective in this research project is to investigate the design and control of a rotor with thrust vector control excited by harmonic motor control, such that a design can be implemented and analyzed.

Let β_c be the elevation angle of the blade tip path plane, corresponding to the maximum teetering angle obtained within a rotation. Let ψ_c be the azimuth angle of maximum blade tilt β_c. The corresponding thrust vector direction is then given by elevation β_c and azimuth ψ_c. The magnitude of thrust is given as T. See Figure 1.6. The control problem is then defined:

- Control the thrust vector magnitude T, as well as direction β_c and ψ_c by harmonically controlling motor torque τ_m.

To be able to achieve the control objective, the rotor mechanism needs to be well understood. Previous model development by Paulos and Yim (2018) will be investigated.

The task of designing and building such system, with the use case and constraints of a MAV in mind, will enable experimental analysis of thrust vector control. A design problem to implement a physical prototype will be split in two parts. Designing and implementing a rotor mechanism that enables thrust vector control. Designing and implementing a motor control system capable of controlling the thrust vector as described.

1.4 Delimitations

The steady state control of the thrust vector will be the focus for all tasks, as this is a minimum requirement. Tracking control of a dynamic thrust vector will not be considered. Further, while the implementation will consider MAV design constraints and optimize for a practical and performant design, the focus for experimentation will be limited to understanding the fundamental behaviour of the rotor.

1.5 Structure of the report

For the theoretical background, two main topics are covered to enable satisfactory design and implementation insights needed for thrust vector control. Chapter 2 Rotor Dynamics will cover modeling of the rotor, focusing on the aerodynamics as well as the hinge mechanism in a rotorcraft perspective. Chapter 3 Field Oriented Motor Control introduces basic motor modeling, such that field oriented control can be covered. Extra focus is put towards MAV specific propulsion motors.

The methodology of this project is divided in two parts. Chapter 4 Design presents the design methodology of the rotor construction. It includes the design of a rotor test rig. Chapter 5 Control presents the motor control methodology. Software and sensor implementation is covered.

In Chapter 6, Experiment Results and Analysis, experimental data is presented, showing the achieved thrust vector control for the designed and implemented rotor.

2

Rotor Dynamics

An analytical model of the articulated rotor is desired to investigate behaviour for both design and control. Paulos and Yim (2018) derived and evaluated a model of the flap and skewed-lag pitch articulated rotor. To analytically model the behaviour of any rotor, aerodynamic needs to be sufficiently modeled and approximated. The theory of aerodynamics for rotor aircraft in the following sections are based on Leutenegger et al. (2016).

2.1 Aerodynamic flight

Aerodynamic forces are generated by an object moving through the air. In this rotor case, the moving object we wish to analyze in terms of aerodynamics is simplified to the blades, while other parts of the rotor are neglected in terms of aerodynamic forces. To model an object moving through air, we need to account for the properties of the atmosphere, which can be summarized by the ideal gas law,

$$p = \rho R T_{\text{air},} \tag{2.1}$$

where p is the pressure, ρ is the air density, R is the ideal gas constant of air and T_{air} is the air temperature. The density and temperature of the atmosphere will in general vary with the altitude, and the pressure will vary accordingly as well. These variables will be important for the aerodynamic effects to be modeled.

Aerodynamic forces are generally complicated, turbulent and unsteady, and several simplifications will be made. The airflow acting on an airfoil section will be assumed to be locally two dimensional, such that analysis can be done locally for infinitesimal airfoil sections.

In each infinitesimal, two dimensional blade element section, the aerodynamic force is split into lift force dL and drag force dD. Lift forces are defined as the aerodynamic force perpendicular to the air inflow given by the local inflow angle ϕ, while the drag forces are defined parallel to the air inflow direction, as seen in Figure 2.1. The chord length c of the blade is defined as the distance between the leading and trailing edge of the blade. The

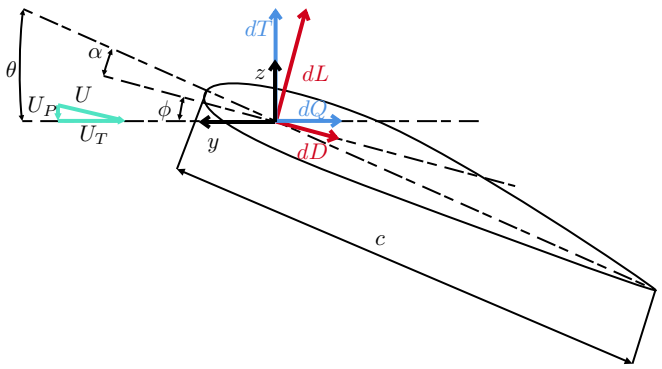

Figure 2.1: Section view of a blade element section.

line through these two points define the chord line. The lift and drag forces are reduced to the point defined $0.25c$ from the leading edge along the chord line. Additionally, there is a moment dM acting on this point. The angle of attack a is defined as the angle between the air inflow and the chord line.

Using a simple drag model, the section lift and drag force can be expressed as

$$\mathrm{d}L = \frac{1}{2}\rho U^2 c_l c \,\mathrm{d}x \tag{2.2}$$

$$\mathrm{d}D = \frac{1}{2}\rho U^2 c_\mathrm{d} c \,\mathrm{d}x, \tag{2.3}$$

where U is the inflow velocity, c_l is the section lift coefficient and c_d is the section drag coefficient. c_l can be expressed in terms of the section lift curve slope a. The lift curve slope of a rotor blade is a measure of how much lift is generated by the blade as the angle of attack increases (Gudmundsson (2014)).

$$a = \frac{dc_l}{d\alpha} \tag{2.4}$$

Assuming a constant lift curve slope, Equation (2.2) can be written as

$$\mathrm{d}L = \frac{1}{2}\rho U^2 a\alpha c \,\mathrm{d}x \tag{2.5}$$

2.2 Modeling of a spinning propeller blade

A common method used to model a spinning propeller blade has been to use blade element momentum theory(BEMT). This combines momentum theory and blade element theory.

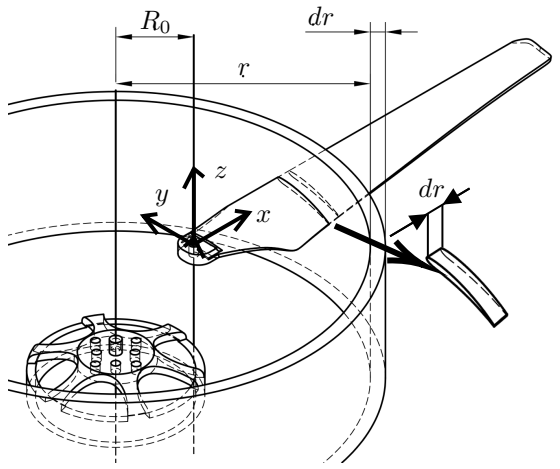

Figure 2.2: Blade element sections constructed along rotor blade. Blade sections with thickness dr are constructed at radius r from the start radius R_0.

2.2.1 Momentum Theory

In momentum theory a control volume is defined by the cylinder reaching far above and below the propulsion disk. The external inflow velocity at a far distance above the propulsion disk is given by v_∞, which equals the climb rate in a rotorcraft situation. The propulsion disk, a boundary layer, is then assumed to produce a thrust force that accelerates the air passing the boundary layer to the sum of the external inflow velocity and the inflow velocity induced by the propeller v_i. At the far wake below the propulsion disk, the air velocity is a higher value v_w. The laws off mass and energy balance can be expressed for this control volume. The equation for the mass flow through a cylinder (Egeland and Gravdahl, 2002, p. 419) is used, and is given by

$$w = \rho v A = \rho(v_\infty + v_i)\pi R^2, \tag{2.6}$$

where w is the mass flow. The air density is considered constant, giving the mass balance

$$\frac{d}{dt}m = \rho A(v_\infty - v_w) \tag{2.7}$$

The momentum balance equation of the control volume can be reduced to

$$f = \frac{dm}{dt}(v_w - v_\infty) = T, \tag{2.8}$$

where T is the total thrust force produced by the propulsion disk, causing a v_i increase of air velocity. The energy balance over the control volume equals the power Tv_i

$$P = fv = Tv_i = \frac{1}{2}\frac{d(m)}{dt}(v_w - v_\infty)^2 \tag{2.9}$$

Inserting Equation (2.8) into Equation (2.9), the far wake velocity is obtained

$$v_w = v_\infty + 2v_i \tag{2.10}$$

Another control volume can be defined by the annular ring at radius r and width dr of the propulsion disk. Using conservation laws as above, thrust force is calculated for each annular ring, and the total thrust can be calculated by integrating over the annular rings along the propulsion disk radius.

2.2.2 Blade element theory

Modeling the blade by the blade element theory method consists of analysis of a single revolving propeller blade. Blade elements are constructed by incrementing sections along the length of the blade, which can be seen in Figure 2.2. Further analysis of a single blade element section shown in Figure 2.1 can be done for a propeller blade spinning at angular speed Ω. The inflow velocity U is defined in terms of components of tangential and perpendicular inflow velocities U_T and U_P. The tangential component is approximated by the blade angular speed and local section radius r

$$U_T \approx \Omega r \tag{2.11}$$

The perpendicular component is approximated by the external inflow velocity v_∞ and the the inflow velocity induced by the propeller v_i.

$$U_P \approx v_i + v_\infty \tag{2.12}$$

The local inflow angle is defined as ϕ in Figure 2.1. This angle will be assumed small, such that it can be approximated as $\phi \approx U_P/U_T$. The local angle of attack a is then found as $a = \theta - \phi = \theta - U_P/U_T$, where θ is the resulting local blade pitch angle. Aerodynamic forces are expressed in terms of incremental thrust and torque, dT and dQ, aligned with the y and z axis. This can be thought of as the thrust force produced, and the force that will induce a torque on the motor.

$$\begin{aligned} \mathrm{d}T &= N_\mathrm{b}(\mathrm{d}L - \phi \mathrm{d}D) \\ \mathrm{d}Q &= N_\mathrm{b} r(\ \mathrm{d}D + \phi \mathrm{d}L) \end{aligned} \tag{2.13}$$

Inserting for α in Equation (2.5), one obtains the section lift and drag forces for the revolving blade

$$\begin{aligned} dL &= \frac{\rho a c}{2} U^2 \left(\theta - \frac{U_P}{U_T}\right) dx \\ dD &= \frac{\rho c}{2} U^2 c_d dx, \end{aligned} \tag{2.14}$$

The drag coefficient is approximated as a single value for all sections, however it will in general vary with the local angle of attack.

By inserting Equation (2.14) in Equation (2.13), lift and drag forces can be calculated by integrating along the blade length, starting at radius R_0.

2.2.3 Disk load and scaling

A possibility with a rotor pitch controlled MAV is to use fewer, larger rotor blades compared to a configuration such as the quadcopter. By employing momentum theory, it is possible to establish a relationship between the ideal power required for hover P, the thrust T and disk area $A = \pi R^2$. At hover, v_∞ is zero. By then inserting Equation (2.7) into Equation (2.8)

$$T = 2\rho A v_i^2 \implies v_i = \sqrt{\frac{T}{2\rho A}} \tag{2.15}$$

Inserting this into Equation (2.9)

$$P = T v_i = T\sqrt{\frac{T}{2\rho A}} \tag{2.16}$$

$$\frac{P}{T} = \sqrt{\frac{T}{2\rho A}}, \tag{2.17}$$

which gives the power per thrust ratio. Disk loading is then defined as T/A. The insight from this relation, is that the lower the disk loading, the more efficient hover can be obtained, requiring less power per thrust. Since the disk loading scales inversely with disk area, a larger disk area compared to the mass of the vehicle will in general give higher hovering efficiency. This relationship can be used for insight about the scale of the vehicle, but it can also be used to compare the efficiency of different rotor configurations. Generally for a similarly sized helicopter and quadcopter in terms of footprint, the helicopter will have a larger disk area compared to the quadcopter, and thus a higher disk load giving a higher hover efficiency.

2.3 Modeling of the cyclic pitch rotor

Paulos and Yim (2018) has developed a model of a hinged, swashplate-less pitch controllable rotor. This model will be presented in this section. The model is developed by considering a single blade with coincident flap and skewed lag-pitch hinges, assuming symmetry between the blades, such that hub inertia and motor torque can be normalized by the number of blades. Dimensional analysis is performed, such that non-dimensional variables are used where possible. This is done to enable general analysis across different rotor scales and system parameters.

The rotor design with a central teetering hinge presents some differences to this model. Assuming that for this design the dynamics of a single blade is modeled, the teetering hinge will act as decoupled flapping hinge, but it will not be coincident with the skewed lag-pitch hinge. Accounting for this difference is not considered in this project.

2.3.1 Canonical coordinate frame

In adopting modeling conventions from rotor aircraft modeling, Paulos and Yim (2018) reparameterizes the skewed hinge rotations in orthogonal flap and lag axes ζ and β. These

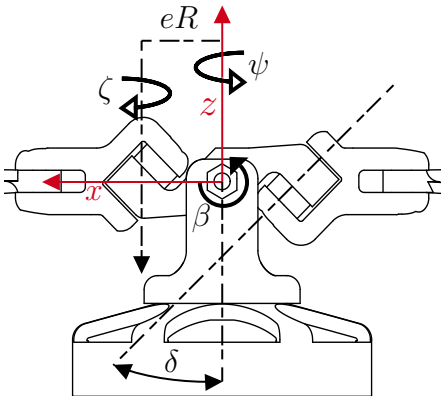

Figure 2.3: Canonical flap ζ and lag β coordinate definitions

axes can be seen in Figure 2.3. The skewed lag-pith axis is skewed by angle δ. The skewed lag-pitch hinge and flap hinge is located at distance eR along the radius, where R is the blade tip radius and $0 < e < 1$ is eccentricity. Note that in Figure 2.3, the canonical flap coordinate β is shown for the teetering hinge rotor, and is not at a distance eR from the center. The re-parametarization consists of hub angle ψ, flap angle β and lag angle ζ. β and ζ are fixed to the rotating hub frame.

2.3.2 Dynamical model

Paulos and Yim (2018) develops generic equations of motion, with generalized coordinates $\mathbf{q} = \begin{bmatrix}\psi & \zeta & \beta\end{bmatrix}^T$.

$$M(\boldsymbol{q})\ddot{\boldsymbol{q}} + C(\boldsymbol{q}, \dot{\boldsymbol{q}})\dot{\boldsymbol{q}} + \boldsymbol{N} = \frac{1}{N_b}\boldsymbol{\tau}_{\text{m}} + \boldsymbol{\tau}_{\text{hinge}} \tag{2.18}$$

The equations of motions follow general modeling with a non-linear inertia matrix $M(\boldsymbol{q})$ and a Coriolis matrix $C(\boldsymbol{q}, \dot{\boldsymbol{q}})$ which appears in a square velocity term. The external forces in the system are the aerodynamic forces $\boldsymbol{N}$, motor torque $\boldsymbol{\tau}_m$ and hinge losses $\boldsymbol{\tau}_{hinge}$.

A linear model is developed, and perturbation variables are introduced to account for the linearization point. The linearization point is defined at

$$\boldsymbol{q}_0 = \begin{bmatrix}\Omega t \\ \zeta_0 \\ \beta_0\end{bmatrix}, \dot{\boldsymbol{q}}_0 = \begin{bmatrix}\Omega \\ 0 \\ 0\end{bmatrix} \tag{2.19}$$

where Ω is the average rotor speed and ζ_0 and β_0 are the flap and lag angles at this average

rotor speed. The perturbation variables are then given as

$$\begin{aligned} \boldsymbol{x} &= \boldsymbol{q} - \boldsymbol{q}_0 = \begin{bmatrix} \tilde{\psi} \\ \tilde{\zeta} \\ \tilde{\beta} \end{bmatrix} \\ \dot{\boldsymbol{x}} &= \dot{\boldsymbol{q}} - \dot{\boldsymbol{q}}_0 = \begin{bmatrix} \tilde{\omega} \\ \dot{\zeta} \\ \dot{\beta} \end{bmatrix} \end{aligned} \tag{2.20}$$

The generalized equations of motions written in perturbation variables are then given by Paulos and Yim (2018) as

$$\boldsymbol{M}\ddot{\boldsymbol{x}} + \boldsymbol{G_C}\dot{\boldsymbol{x}} + \boldsymbol{K_C}\boldsymbol{x} + \boldsymbol{C}_0 + \boldsymbol{N} = \frac{1}{N_b}\boldsymbol{\tau}_m + \boldsymbol{\tau}_{\text{hinge}} \tag{2.21}$$

where G_C is the effective gyroscopic coefficient matrix, K_C is the effective stiffness coefficient matrix and C_0 is a constant term. These terms in addition to $\boldsymbol{M}$ are approximations at the linearization point. To reduce the scope of further analysis, the aerodynamic term and the motor torque term entering this model are considered for further investigation.

2.3.3 Aerodynamic forces

The aerodynamic forces are modeled with BEMT. We want to express Equation (2.13) for the rotor in terms of perturbation variables $\boldsymbol{x}$ and $\dot{\boldsymbol{x}}$, and then calculate the aerodynamic moments about $\boldsymbol{x}$.

A single rotating blade is considered at the linearization point. A non-dimensional spanwise coordinate $0 \leq \xi \leq 1$ is introduced, with $dx = Rd\xi$. The blade induced inflow velocity v_i is expressed in terms of $\dot{\boldsymbol{q}}$. These relations enter in Equation (2.12) and Equation (2.11), such that inflow velocity can be defined spanwise from $R_0 = eR$ to R.

$$\begin{aligned} U_P &= v_\infty + R(\xi - e)\dot{\beta} \\ U_T &= R\xi(\Omega + \tilde{\omega}) - R(\xi - e)\dot{\zeta} \end{aligned} \tag{2.22}$$

Incremental section forces dT and dQ can now be expressed. Paulos and Yim (2018) defines incremental forces along positive z and y direction, while the dT and dQ directions defined in Figure 2.1 will be used here. dT is aligned with the z-axis in Figure 2.3. The y-axis is defined as in Figure 2.2, such that dQ is defined in negative y direction. Inserting for U_P and U_T in Equation (2.13), and neglecting higher order terms of $\dot{\boldsymbol{q}}$, the incremental forces are found by Paulos and Yim (2018).

$$
\begin{aligned}
dT &= \frac{\rho a c \Omega^2 R^3}{2}\left\{-\left(1+\frac{c_d}{a}\right)\xi\frac{v_\infty}{\Omega R}+\theta\left(\xi^2\right)+\frac{\tilde{\omega}}{\Omega}\left(2\theta\xi^2-\left(1+\frac{c_d}{a}\right)\xi\frac{v_\infty}{\Omega R}\right)\right.\\
&\left.-\frac{\dot{\zeta}}{\Omega}\left(2\theta\xi(\xi-e)-\left(1+\frac{c_d}{a}\right)(\xi-e)\frac{v_\infty}{\Omega R}\right)-\frac{\dot{\beta}}{\Omega}\left(\left(1+\frac{c_d}{a}\right)\xi(\xi-e)\right\}d\xi\right.\\
dQ &= \frac{\rho a c \Omega^2 R^3}{2}\left\{\frac{c_d}{a}\xi^2\frac{v_\infty^2}{\Omega^2R^2}+\theta\left(\xi\frac{v_\infty}{\Omega R}\right)+\frac{\tilde{\omega}}{\Omega}\left(2\frac{c_d}{a}\xi^2+\theta\xi\frac{v_\infty}{\Omega R}\right)\right.\\
&\left.-\frac{\dot{\zeta}}{\Omega}\left(2\frac{c_d}{a}\xi(\xi-e)+\theta(\xi-e)\frac{v_\infty}{\Omega R}\right)+\frac{\dot{\beta}}{\Omega}\left(\theta\xi(\xi-e)-2(\xi-e)\frac{v_\infty}{\Omega R}\right)\right\}d\xi
\end{aligned}
\tag{2.23}
$$

These incremental forces result in moments about the generalized coordinates, and can be found by integrating along the blade length.

$$
\begin{aligned}
\boldsymbol{M}_{\psi_{\text{aero}}} &= -R\int_0^1 \xi \mathrm{d}Q\\
\boldsymbol{M}_{\zeta_{\text{aero}}} &= R\int_0^1 (\xi-e)\mathrm{d}Q\\
\boldsymbol{M}_{\beta_{\text{aero}}} &= R\int_0^1 (\xi-e)\mathrm{d}T
\end{aligned}
\tag{2.24}
$$

The final expression for the aerodynamic moments $\boldsymbol{N}$ that enters in the generalized equations of motions is collected as

$$
\boldsymbol{N} = \begin{bmatrix} -\boldsymbol{M}_{\psi_{\text{aero}}} \\ -\boldsymbol{M}_{\zeta_{\text{aero}}} \\ -\boldsymbol{M}_{\beta_{\text{aero}}} \end{bmatrix}
\tag{2.25}
$$

The external inflow velocity v_∞ appearing in Equation (2.23) can be expressed in terms of the climb rate for a rotorcraft. For a rotorcraft with zero climb rate, Paulos and Yim (2018) uses the following relation for inflow velocity

$$
\frac{v_\infty}{\Omega R} = \frac{a\sigma}{16}\left(\sqrt{1+\frac{32\theta}{a\sigma}}\,\xi - 1\right)
\tag{2.26}
$$

where σ is the rotor solidity, $\sigma = N_b c/(\pi R)$.

2.3.4 Motor model and control

Paulos and Yim (2018) models the motor as a simplified DC-motor. The general DC motor model with motor torque proportional to the current above the no load current is used.

$$
\begin{aligned}
\tau_m &= K_e\left(i - i_0\right)\\
i &= \frac{1}{R_{\text{ohm}}}\left(V - K_e\dot{\psi}\right)
\end{aligned}
\tag{2.27}
$$

where K_e is the electrical constant of the motor, R_{ohm} is the resistance, V is the motor input voltage and i_0 is the no load current.

The motor is controlled by a voltage input. A given average motor speed can be tracked by a proportional integral controller (PI-controller). Paulos and Yim (2018) proposes to modulate the harmonic signal as a sinusoidal voltage perturbation. The control law is defined as

$$\begin{aligned} V =& - K_P(\dot{\psi} - \Omega) - K_I \int (\dot{\psi} - \Omega)\mathrm{d}t + \tilde{V} \\ \tilde{V} =& A\cos(\psi) \end{aligned} \tag{2.28}$$

where K_p and K_i are constants for the PI-controller controller, Ω is the average motor speed and A is the amplitude of the sinusoidal voltage signal. The resulting motor torque is expressed by inserting Equation (2.28) in Equation (2.27)

$$\tau_m = -\frac{K_P K_e}{R_{\mathrm{ohm}}}(\dot{\psi} - \Omega) - \frac{K_I K_e}{R_{\mathrm{ohm}}} \int (\dot{\psi} - \Omega)\mathrm{d}t + \frac{K_e}{R_{\mathrm{ohm}}}\tilde{V} - \frac{K_e^2}{R_{\mathrm{ohm}}}\dot{\psi} - K_e i_0 \tag{2.29}$$

At equilibrium, where $\dot{\psi} = \Omega$, the constant torque τ_{m_0} needed to achieve $\dot{\psi} = \Omega$ with $\tilde{V} = 0$ results in

$$\tau_{m_0} = -\frac{K_I K_e}{R_{\mathrm{ohm}}} \int (\dot{\psi} - \Omega)\mathrm{d}t - \frac{K_e^2}{R_{\mathrm{ohm}}}\Omega - K_e i_0 \tag{2.30}$$

This can be written in terms of perturbation variables previously defined. Paulos and Yim (2018) defines the integral of speed perturbation to be equal to $\tilde{\psi} = \psi - \Omega t$.

$$\tilde{\tau}_m = -\left(K_P + K_e\right)\frac{K_e}{R_{\mathrm{ohm}}}\tilde{\omega} - K_I \frac{K_e}{R_{\mathrm{ohm}}}\tilde{\psi} + \frac{K_e}{R_{\mathrm{ohm}}}\tilde{V} \tag{2.31}$$

This term, when written in perturbation variable $\boldsymbol{x}$ and $\dot{\boldsymbol{x}}$ enters Equation (2.21).

3

Field Oriented Motor Control

3.1 AC synchronous motors

For MAV propulsion, AC synchronous motors with permanent rare-earth magnets are commonly used, while brushed DC motors have been used primarily for extremely low cost vehicles. Compared to brushed DC motors, AC synchronous motors eliminate the mechanical brush commutator, achieving higher power density, better dynamical performance and efficiency (Leonhard (2001)).

Two different designs of AC synchronous motors with permanent magnets will be analyzed, permanent magnet synchronous motors (PMSM), and brush-less DC motors (BLDCM). The main difference between the PMSM and BLDCM is the shape of the back-electromotive force (EMF) waveform. PMSM has windings designed for a sinusoidal back-EMF, and BLDCM has windings designed for a trapezoidal back-EMF waveform (Leonhard (2001)). Off the shelf motors typically used for propeller driven MAVs are commonly BLDCM. The reason for the back-EMF waveform of BLDCM is that it is suited for a simple, more economical 6-step control method (Leonhard (2001)). For PMSM, FOC is a common control technique, but BLDCM can still benefit from FOC. As the electrical and mechanical dynamical model is otherwise identical between these motor types, PMSM will be considered for modeling, before discussions of differences between PMSM and BLDCM.

3.2 PMSM model

A PMSM with three stator windings, corresponding to phases a, b, c will be considered. The stator phases has corresponding currents $\boldsymbol{i}_{abc} = \begin{bmatrix} i_a & i_b & i_c \end{bmatrix}^T$, voltages $\boldsymbol{u}_{abc} = \begin{bmatrix} u_a & u_b & u_c \end{bmatrix}^T$ and fluxes $\boldsymbol{\varphi}_{abc} = \begin{bmatrix} \varphi_a & \varphi_b & \varphi_c \end{bmatrix}^T$. An illustration of a single pole pair PMSM with external rotor is given in Figure 3.1. The permanent magnets lie in the rotor, while the phase windings lie in the stator. Interior rotor PMSMs are most common in industry, but MAVs mostly have exterior rotors. It does not present a difference for a

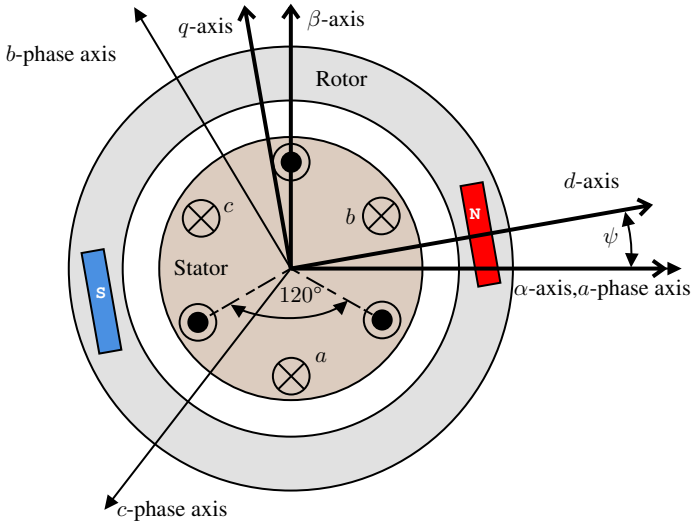

Figure 3.1: Exterior rotor PMSM with single pole pair.

simplified model. The rotor position ψ is given in relation to the a-phase axis, and the mechanical rotor speed $\omega = \dot{\psi}$ is assumed to be positive to simplify modeling. The phase quantities are assumed to be balanced due to symmetry (Leonhard (2001)), such that

$$\begin{aligned} i_a + i_b + i_c &= 0 \\ u_a + u_b + u_c &= 0 \\ \varphi_a + \varphi_b + \varphi_c &= 0 \end{aligned} \tag{3.1}$$

The rotor electrical angle is given as $\psi_e = N_p \psi$, where N_p is the number of pole pairs. The number of poles of the PMSM will typically be equal to the number of permanent magnets in the rotor. Figure 3.1 shows a PMSM with a single pole pair, such that the rotor mechanical angle ψ is aligned with the electrical angle ψ_e.

A general AC synchronous motor stator voltage laws are given by Leonhard (2001)

$$\frac{d\boldsymbol{\varphi}_{abc}}{dt} = \boldsymbol{u}_{abc} - R_{ohm}\boldsymbol{i}_{abc} \tag{3.2}$$

where R_{ohm} is the stator winding resistance, such that the voltage is dissipated as resistive winding losses and contributions to the stator fluxes. The rotor flux is given by the permanent magnets in the rotor. The rotor flux components $\boldsymbol{\varphi}_r$, written in the stationary stator frame will rotate with rotor electrical angle ψ_e. $\boldsymbol{\varphi}_r$ can be written as (Bosso et al. (2021))

$$\boldsymbol{\varphi}_r = \varphi_e \begin{bmatrix} \cos(\psi_e) \\ \cos(\psi_e - 2\pi/3) \\ \cos(\psi_e + 2\pi/3) \end{bmatrix} \tag{3.3}$$

where φ_e is the nominal rotor flux amplitude. The stator flux $\boldsymbol{\varphi}_{abc}$ consists of two components, a stator current component and a rotor flux component.

$$\boldsymbol{\varphi}_{abc} = \boldsymbol{\varphi}_r + L\boldsymbol{i}_{abc} \tag{3.4}$$

By time differentiating Equation (3.4)

$$\frac{d\boldsymbol{\varphi}_{abc}}{dt} = -\varphi_e \begin{bmatrix} \sin(\psi_e) \\ \sin(\psi_e - 2\pi/3) \\ \sin(\psi_e + 2\pi/3) \end{bmatrix} \dot{\psi_e} + L\frac{d\boldsymbol{i}_{abc}}{dt} \tag{3.5}$$

the current dynamics are obtained by inserting Equation (3.2) in Equation (3.5).

$$\begin{aligned} \frac{d\boldsymbol{i}_{abc}}{dt} =& \frac{\boldsymbol{u}_{abc}}{L} - \frac{R_{ohm}\boldsymbol{i}_{abc}}{L} + \frac{\varphi_e}{L} \begin{bmatrix} \sin(\psi_e) \\ \sin(\psi_e - 2\pi/3) \\ \sin(\psi_e + 2\pi/3) \end{bmatrix} \dot{\psi_e} \\ \dot{\psi_e} =& \omega_e \end{aligned} \tag{3.6}$$

3.3 Coordinate transformations

The stator winding currents, voltages and fluxes will be represented in different frames, which will be convenient for control.

3.3.1 Clarke transformation

The abc quantities can be transformed to a stator fixed, orthogonal two coordinate frame $\alpha\beta$ by the Clarke transform (O'Rourke et al. (2019)). The Clarke transform is given by

$$\boldsymbol{T}_C = \frac{2}{3} \begin{bmatrix} 1 & -\frac{1}{2} & -\frac{1}{2} \\ 0 & \frac{\sqrt{3}}{2} & -\frac{\sqrt{3}}{2} \\ \frac{1}{2} & \frac{1}{2} & \frac{1}{2} \end{bmatrix} \tag{3.7}$$

This transformation preserves amplitudes as its determinant is 1. Due to the balanced quantities from Equation (3.1), we get the two-coordinate $\alpha\beta$ frame by noticing that the last coordinate after applying the Clarke transform always equals zero. By using this simplification, the i_α and i_β currents are expressed as

$$\begin{bmatrix} i_\alpha \\ i_\beta \end{bmatrix} = \frac{2}{3} \begin{bmatrix} 1 & -\frac{1}{2} & -\frac{1}{2} \\ 0 & \frac{\sqrt{3}}{2} & -\frac{\sqrt{3}}{2} \end{bmatrix} \begin{bmatrix} i_a \\ i_b \\ i_c \end{bmatrix} \tag{3.8}$$

As seen in Figure 3.1, the α-axis is stator fixed and aligned to the a-phase axis.

3.3.2 Park transformation

A rotor fixed, orthogonal two coordinate direct-quadrature frame dq is defined, with the d-axis aligned with the rotor electrical angle ψ_e (O'Rourke et al. (2019)). A transformation from the $\alpha\beta$-frame to the dq reference frame is then simply a 2D rotation by ψ_e. The transformation can be expressed with a 2D rotation matrix

$$\begin{bmatrix} i_d \\ i_q \end{bmatrix} = \begin{bmatrix} \cos(\psi_e) & \sin(\psi_e) \\ -\sin(\psi_e) & \cos(\psi_e) \end{bmatrix} \begin{bmatrix} i_\alpha \\ i_\beta \end{bmatrix} \tag{3.9}$$

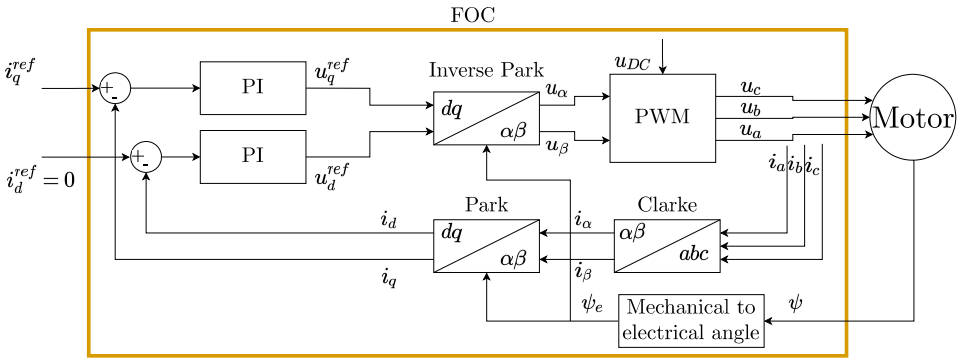

Figure 3.2: Block diagram of Field oriented control algorithm

This rotation will be referenced as the Park transformation in the following sections, however the total transformation from abc quantities to dq frame is sometimes referenced as the Park transform (O'Rourke et al. (2019)).

3.4 Field oriented control

The main idea of FOC is to do feedback current control in the rotor fixed frame dq. The current dynamics in Equation (3.6) can be expressed in the dq-frame by applying the Clarke and Park transform. After applying some trigonometric identities, the result of this transformation can be written as

$$\begin{aligned} \frac{di_d}{dt} &= \frac{u_d}{L} - \frac{R_{ohm} i_d}{L} + \dot{\psi}_e i_q \\ \frac{di_q}{dt} &= \frac{u_q}{L} - \frac{R_{ohm} i_q}{L} + \frac{\varphi_e}{L} + \dot{\psi}_e i_d \end{aligned} \tag{3.10}$$

In this frame, currents and voltages vary slowly and can be controlled at a much lower bandwidth compared to the stator frame due to the independence of rotor electrical position. Another convenient feature of the dq frame is that d and q currents will independently contribute to the flux and torque respectively. This is similar to the dynamics of a DC motor. The electrical torque in a PMSM in the dq-frame is given as (Bosso et al. (2021))

$$\tau_m = \frac{3}{2} i_q N_p \varphi_e \tag{3.11}$$

This relation can be expressed in terms of a torque constant $k_T = N_p \varphi_e$ with SI unit $[\frac{Nm}{A}]$, or in terms of the back-EMF constant $k_e = N_p \varphi_e$ with unit $[\frac{V}{rad/s}]$. k_e is also called the motor electrical constant.

$$\tau_m = \frac{3}{2} i_q k_e \tag{3.12}$$

This result shows that the torque dynamics in terms of quadrature current i_q is similar to that of a DC-motor.

3.4.1 FOC algorithm

The remaining problem is to find and apply the phase voltages $\boldsymbol{u}_{abc}$ that will result in the dq reference current. Figure 3.2 shows an overview of the FOC algorithm. The current controller of the motor operates in rotor frame currents i_q and i_d. A control objective of FOC is to maximize the torque per ampere. This can be achieved by controlling the direct current i_d to zero, and using the quadrature current i_q as the reference. A quadrature current reference is given as input to the current controller, which outputs voltage references in the dq rotor fixed frame. To perform feedback current control, the current needs to be measured or estimated. By directly measuring phase currents i_a, i_b, i_c, as well as measuring or estimating ψ_e, Clark and Park transformations can be applied to reconstruct measured dq currents for the current loop. The output from the current controller, quadrature and direct voltage references u_q^{ref} and u_d^{ref} are transformed to $\alpha\beta$-frame. Pulse width modulation (PWM) of the DC supply voltage u_{DC} is used to generate the phase voltages to be applied to the motor phases.

Torque control is the obtained by the relation

$$i_q^{ref} = \frac{2}{3N_p\varphi_e}\tau_m^{ref} \tag{3.13}$$

such that a reference torque τ_m^{ref} can be tracked by calculating the equivalent quadrature current reference i_q^{ref} for the current loop, while keeping the direct current reference i_d^{ref} zero.

3.5 6-step BLDCM control

The 6-step algorithm, also called trapezoidal control, exploits the specifically designed back-EMF characteristic of BLDCM, and is widely used for MAV motor control. Some variation of this algorithm is used by the motor controller in Qin et al. (2022). For the 6-step algorithm, one motor phase is given a PWM-driven voltage, one phase is driven to 0, and one phase is kept floating at any time moment (Bosso et al. (2021)). Current only flows between the two non floating phases, and Equation (3.1) conveniently restricts the control problem. The motor is divided in a sextant, where the controlled phase is updated at every crossing. The crossings can be detected by measuring the back-EMF such that a crossing happens when the open phase voltage crosses zero compared to neutral. The duty-cycle of the PWM signal then gives the back-EMF oriented current vector, which is used to control the motor speed. In this technique, the mechanical angle of the motor is not needed, the electrical angle is rather estimated based on the zero-crossings. Another advantage of the 6-step algorithm is that it is completely parameter free, making it seamless to apply to different motors.

3.6 FOC for BLDCM

Field oriented control has been shown for PMSM, however the motor that will be used is a BLDCM. FOC can be applied in the exact same manner for BLDCM. The main difference

will be torque ripple due to the mismatch between sinusoidal drive current from FOC and the trapezoidal back-EMF of BLDCM. (Leonhard, 2001, c.14) states that the 6-step algorithm of BLDCM suffers from torque ripple due to the difficulty of manufacturing a BLDCM with a perfect trapezoidal back-EMF. Bosso et al. (2021) investigates the back-EMF of two different BLDCMs designed for MAV use. It is apparent that the back-EMF waveforms of the tested motors is closer to a sinusoidal than trapezoidal. Bosso et al. (2021) then validates experimentally that for a specific BLDCM, T-Motor Antigravity 4006, a FOC approach outperforms a 6-step algorithm in efficiency by a small margin. The tests were performed by operating the motor with a 13 inch propeller at different constant speeds. Efficiency were measured by considering the total power compared to the resistive losses in the windings, computed from the measured winding resistance. In particular, the efficiency gains were measured to be 0.4%, 0.77% and 0.98% respectively for steady propeller spinning at 3000, 4500 and 6000 rpm.

4

Design

4.1 Design of rotor

The designed thrust vector controllable rotor derives closely from the rotor design of Qin et al. (2022). The rotor configuration in Figure 4.1 consists of a single teetering hinge and positive and negative 45 degree skewed lag-pitch hinges. A central hub connects the mechanism to the motor, and acts as a mount for the teetering hinge. The teetering hub revolves around the teetering hinge, and connects to the two side hubs. The side hubs are connected to the teetering hub through the skewed lag-pitch hinges. Qin et al. (2022) uses two different types of bearings to achieve low friction, and these are used here. Each of the three hinges has two ball bearings to support radial load. For the teetering hinge, two thrust bearings clasp the teetering hub such that axial load can be supported between the central hub and the teetering hub. For the side hubs, only one thrust bearing for axial load is used. The argument given by Qin et al. (2022) is that when the rotor is spinning, the lateral component of the centrifugal force will act on the side hubs, such that they are forced against the single thrust bearing.

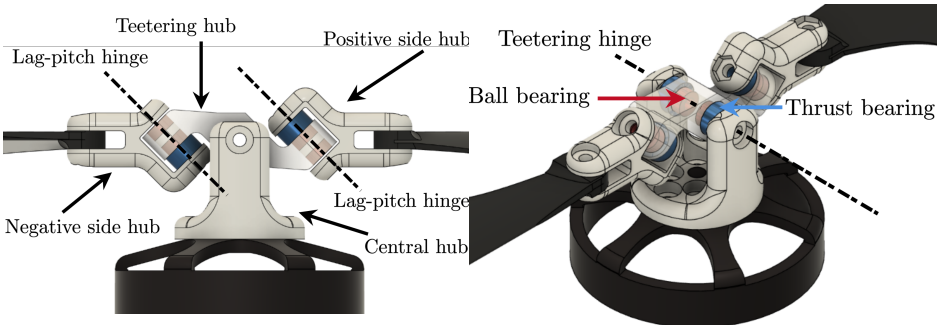

Figure 4.1: Annotated rotor design. Ball bearings are colored red, thrust bearings are colored blue.

Table 4.1: Dimensional specification of mechanical parts for the pitch controllable rotor. Bearing dimensions are given in (inner diameter) x (outer diameter) x (heigth)

Part	Dimension
Propeller	13-inch
Thrust bearing	3mm x 8mm x 3.5mm
Ball bearing	3mm x 6mm x 2.5mm
Bolts	M3

Figure 4.2: 3D-printed rotor assembly.

The design consists of choice of hardware such as hinges and bolts, as well as geometry that connects these parts and the motor together.

4.1.1 Mechanical design specifications

To develop design specifications for the rotor, potential constraints were first identified. The first constraint were choosing rotor hinge configuration, a T-Motor MF1302 propeller and MN5006 motor, the same as used by Qin et al. (2022). This sets the scale of forces and rotational speed. A second constraint is the availability of miniaturized bearings. The smallest thrust bearing that were readily available were identified as a constraint, and chosen. The mechanical parts chosen and their dimensions are listed in Table 5.2. This provides the geometrical specifications for hardware interfaces in the 3D-modeled parts.

The geometry of the 3D-modeled parts will limit the maximum hinge angles. Given a desired maximum thrust vector angle β_c, the maximum teetering hinge angle is equal to β_c. The skewed lag-pitch angle will depend on the dynamics of blade lag and flap.

4.1.2 3D-modeled parts

When designing the 3D-modeled parts, accurate tolerances and correct interfacing to the hardware specified is crucial. Additionally, the parts need to withstand the forces during operation. A rapid prototyping approach were chosen to experimentally determine suitable dimensions. An initial design were drawn in computer aided design software Fusion 360.

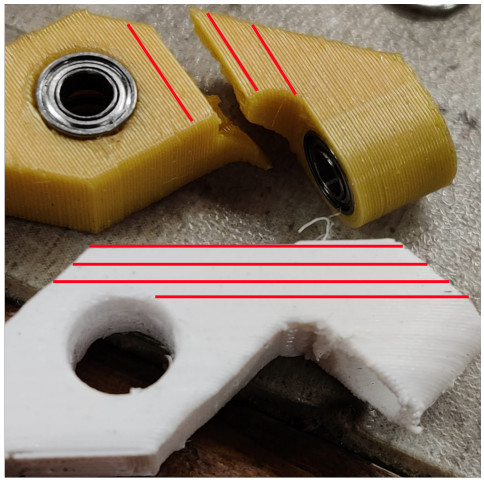

Figure 4.3: Comparison between layer orientation of 3D-printed teetering hub. Layer lines are illustrated by the drawn lines. Top part: Hub that broke under operation. Bottom part: Revision of design with improved layer orientation.

A parametric design were made, such that important dimensions and tolerances could be rapidly updated. By 3D-printing these parts in plastic, design revisions could be evaluated rapidly, and at low cost, for hardware interfaces, tolerances and strength. Several revisions were made until satisfactory dimensions were determined.

4.1.3 Prototype fabrication

Several different materials and manufacturing methods could be used to fabricate the modeled rotor parts. 3D-printing the prototype rotor was chosen, as discovery of potentially needed design revisions were possible. The strength and light weight were also satisfactory for a prototype with this method. A Fused Deposition Modeling extrusion printing machine were used, and PETG plastic were chosen for its strength, rigidity and ease of printing. The final produced part can be seen in Figure 4.2

Due to the layer-by-layer extrusion technique, the parts have anisotropic properties, the strength of the parts varies with the direction of the layers. Generally, the strength between the bonds of layers are weaker than the strength along layer lines. Figure 4.3 illustrates two different choices of layer orientations. The upper part, which broke during rotor acceleration, has layers oriented perpendicular to the length of the part, splitting the part at the narrowest section. The part has broken primarily between the layer lines, which is also perpendicular to the centrifugal force that will act on the part. The bottom part has layers running along the direction of the part, and should therefore be better at withstanding these forces.

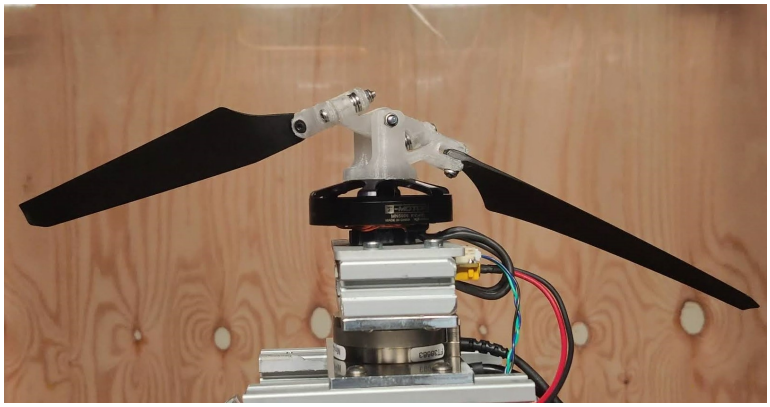

Figure 4.4: Rotor at rest position.

4.1.4 At rest behaviour

Another consideration for the rotor design is the hinge configuration at rest, which can be seen in Figure 4.4. For the negative lag-pitch coupled blade, the center of mass of the blade and side hub lies below the lag-pitch hinge axis. A zero skewed lag-pitch angle is a stable equilibrium in this case, and the blade will rest with zero skewed lag-pitch angle. For the positive skewed lag-pitch coupled blade, the center of mass of the blade and side hub lies above the lag-pitch hinge axis. In this case, the zero skewed lag-pitch angle is an unstable equilibrium, causing the blade to rotate to one of the end positions of the lag-pitch hinge. By doing so, the blade moves closer to the center of the rotor, shifting the center of mass of the total assembly away from center. This causes the rotor to rotate about the teetering hinge towards the negative lag-pitch coupled blade. The problem with this at rest behaviour, is that the rotor has to be started from the most extreme teetering angle. Thus it will need full clearance from potential obstructions while rotating at this extreme.

4.1.5 Vibrations

The at rest behaviour illustrates another potential problem for the mechanism. Assume that the mechanism is driven to a specific blade tilt angle β_c. As the blades lag and pitch through the skewed lag-pitch hinge, the center of mass for each blade changes in the rotor fixed frame. As long as both blades lag and pitch with the same amplitude at each time moment, the center of mass of the mechanism will remain in the center of the rotation. Additionally, with equal lag-pitch hinge amplitudes for the two blades, the resulting blade tilt about the teetering axis will be equal when each blade passes the same point within a rotation. If there is a difference in the lag-pitch hinge amplitudes for each of the two blades at the same point within a rotation, two different blade tilt angles are obtained. In that case, a first harmonic oscilating rotor blade tilt behaviour occurs, with a frequency of the average motor speed Ω. To reduce this effect, the two side hubs and blades needs to be as symmetrical as possible. Additionally, the friction in the lag-pitch hinges should also be equal. Qin et al. (2022) identified the friction asymmetry issue, and proposed the single

thrust bearing and freely rotating side hubs as a potential mitigation of asymmetric hinge friction.

4.2 Test rig

A custom test rig were designed and built to allow experimentation. Several requirements were considered:

- The rotor should be as rigidly attached to the ground as possible, such that flex in the mounting structure is not affecting the system.
- The rotor should be placed such that airflow is minimally obstructed by the rig.
- A protective cage should be constructed around the rotor.

A construction out of 2020 aluminium extrusion profiles were designed. Four profiles are mounted vertically on an aluminium base plate, with horizontal top profiles where sensors and the rotor can be attached. The profiles are supported by four 30 degree skewed supporting profiles to stiffen the vertical construction. In absence of off the shelf 30 degree profile brackets, 3D-printed brackets were designed and used. Heavy weights are placed on the aluminum base plate to hold it down in anticipation of lifting force.

A protective cage is constructed out of 4mm thick acrylic sheets. 3D-printed corner clamps holds these together, and makes it easy to disassemble and store.

To mitigate airflow disturbance from ground effect, the rotor is mounted at a vertical distance from the ground. The protective cage has large openings at the bottom to allow the air to exit here.

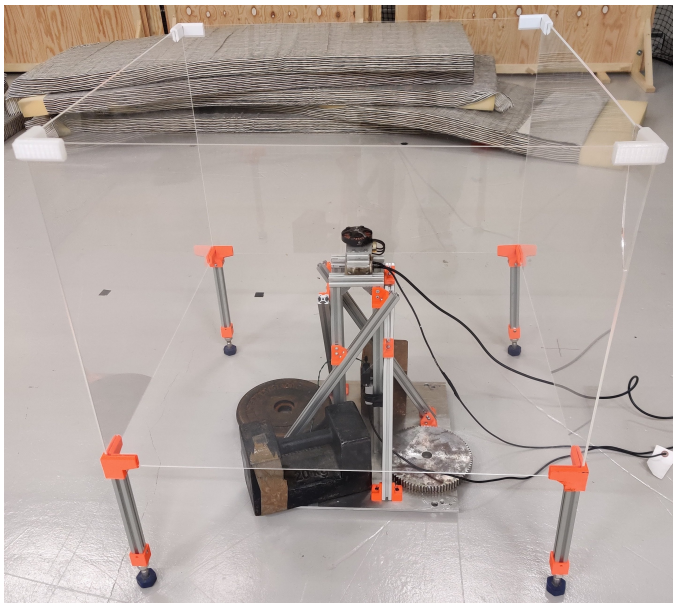

Figure 4.5: Rotor test rig with protective cage.

5

Control

5.1 Motor driver hardware

A field oriented controller within design specifications of the chosen motor and propeller is chosen. Unlike the 6-step control algorithm implemented in most off the shelf BLDCM drivers, FOC requires certain parameters of the motor, as well as tuning. For this reason, FOC drivers are often designed for a specific motor. A configurable field oriented controller with open source firmware were chosen to have control over parameters, and not rely on the manufacturer for motor integration. The Moteus r4.11 controller were chosen. It is reasonably electrically and mechanically dimensioned for the motor and load, weighing 14.2g with a peak phase current rating of 100A and a peak electrical power rating of 500W. The continuous load rating will depend on cooling and will be experimentally tested. The circuit board has an integrated hall effect absolute magnetic encoder for measuring the rotor position, such that the whole unit is mounted below the motor.

The FOC algorithm is not relatively computationally cheap and should run at a high rate. The Moteus controller uses a 32-bit STM32G4 microprocessor in the main microcontroller. The internal firmware runs a FOC loop with similar structure as shown in Figure 3.2. Additionally an outer configurable PID position or speed loop is implemented on the controller. The whole control system runs at an update rate of 30kHz.

5.1.1 Rotor position measurement

An AS5047P magnetic encoder with an angular resolution of $2\pi/4096$ is integrated in the Moteus controller, which communicates via SPI to the main microcontroller at 12MHz and is sampled at every iteration. In comparison, Qin et al. (2022) uses the AS5600 magnetic encoder with a slower I2C protocol, were they achieve 920Hz sampling rate of position measurements.

To measure the position of the rotor, a diametrically magnetized magnet is used. A magnetization across the diameter allows the direction of the magnetic field to be used as a measure of the rotor position. The drive shaft of the motor extends through the center of

(a) Motor and motor driver mounted

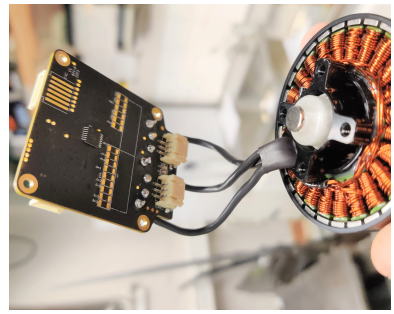

(b) Motor and motor driver unmounted

Figure 5.1: Motor with motor driver and diametrically magnetized magnet for rotor position measurement

the stator down to the motor mounting base, where such a magnet can be mounted. For optimal performance, the magnet should be placed accurately in relations to the encoder, which resides in a surface mounted chip package on the Moteus controller board. A 3D-printed magnet guide jig were designed and used to achieve accurate positioning. See Figure 5.1. Initial testing with a manual, off center magnet mount resulted in excessive audible noise from the motor.

As the measurements from the encoder are noisy, a filter is used for mechanical position, and this filtered position is used to determine mechanical speed ω to be used in velocity control. A computationally efficient all-digital phase locked loop filter is implemented by the Moteus driver, and the bandwidth can be configured.

An offset position is defined such that the positive blade aligns with azimuth angle zero as defined in Section 1.3.

5.1.2 Communication

Motor commands needs to be sent to the controller, and position feedback and other data needs to received. The Moteus controller has an interface using the Controller Area Network Flexible Data-rate (CAN-FD) protocol, capable of up to 5Mbps. A CAN-FD to USB adapter is used to connect the computer to the motor driver.

5.1.3 Power

A lithium ion polymer battery with 6 cells in series (6s) is used to supply DC voltage to the motor driver. The Moteus controller has a rated maximum DC input voltage of 44V, while the T-Motor Antigravity MN5006 motor is rated for 4s-6s lithium ion polymer batteries. The battery has a rated capacity of 1.8Ah and a high discharge rating, with a peak discharge current rating of 180A. This is well above what the single rotor will draw in current, but it results in a more stable DC voltage under load compared to a lower discharge rating.

Table 5.1: Measured T-Motor MN5006 motor parameters

Parameter	Value
Motor electrical constant K_e	0.014 V/(rad/s)
Stator resistance R_{ohm}	0.108 ohm
Stator inductance L	1.409×10^{-5} H
Number of pole pairs N_p	14

5.2 Parameter estimation

Several motor parameters is needed for the FOC algorithm, and is in this case not given by the manufacturer. Estimation of stator inductance L, stator resistance R and back EMF constant K_e was performed. To estimate these parameters, a calibration script bundled with the Moteus controller were used. The details of this script is described below.

Stator resistance is measured by applying different u_d voltages, measuring the corresponding current and using Ohm's law to calculate the average resistance. Stator inductance is measured by applying a u_d reference and measuring the rate of change of current. Then the definition of inductance, $L = u(t)/\frac{di}{dt}$ can be used. d-axis voltage is used in both cases, such that there is no torque applied to the motor, resulting in a zero rotor speed. In the case of resistance measurement, there are no mechanical losses. In the case of inductance measurements, there are no mutual inductances.

The motor velocity constant k_v, defined as $k_v = \omega_{noload}/u$ is estimated by the calibration script by applying a quadrature voltage u_q and measuring the motor mechanical speed ω. This was performed without any propeller or similar connected to the motor.

The back-EMF constant k_e appearing in Equation (3.12) is estimated as $k_e = 1/k_v$ under the assumption of no mechanical losses. As there are clearly losses when spinning the motor, this method is not particularly accurate.

Alternatively to how k_e was estimated in this project, a more direct method is possible. By spinning the motor externally, operating it as a generator, a relation between rotational velocity and back-EMF can be established, circumventing the mechanical losses. This method is used by Bosso et al. (2021).

5.3 Motor control law

Previous implementations of cyclical pitch with harmonic motor control such as by Paulos and Yim (2018) and Qin et al. (2022) have used a PI speed controller outputting voltage, with feedforward voltage as harmonic modulator. It would be possible to implement this scheme using FOC by removing the current controller, and directly controlling quadrature voltage u_q as the voltage in Equation (2.28). This has disadvantages. With FOC, we want to achieve smooth and maximum torque, which is given by the current in Equation (3.12). This is especially important when controlling torque within bounds, although that is not necessarily needed in this propeller use case. An advantage of using a current controller is that control of electrical and mechanical dynamics are decoupled, and can be tuned separately. Another reason to use the current loop in this case is in software limitations.

The built in speed PI-controller in the Moteus firmware can only be used as an input to the current controller. It is advantageous to run as much of the high rate control loop as possible on the microcontroller on the Moteus controller.

The control objective is to control the thrust vector magnitude T and direction β_c and ψ_c. Paulos and Yim (2018) finds that there is an approximately linear relationship between the amplitude A of the modulated sinusoidal voltage in Equation (2.28) and maximum tilt angle β_c. Paulos et al. (2018) and Qin et al. (2022) uses this fact to establish a linear relationship between β_c and A.

$$\beta_c = K_a A \tag{5.1}$$

where K_a is a constant. This relationship will be investigated experimentally. For the azimuth angle of maximum blade tilt, Paulos and Yim (2018) finds that ψ_c lags the modulated input voltage $\tilde{V}$ by an angle, defined ψ_K here. Paulos et al. (2018) uses this relationship together with Equation (5.1) to propose an updated modulated voltage control law from Equation (2.28).

$$\tilde{V} = (\tilde{V}_{min} + K_a A)\cos(\psi - \psi_c - \psi_K) \tag{5.2}$$

where $\tilde{V}_{min}$ is the minimum amplitude required to overcome static friction in the pin hinges used.

Qin et al. (2022) uses a slightly different control law. As radial and axial low friction bearings are introduced, no minimum amplitude is assumed to be needed for blade tilt response. The ψ_K lag is set to be a function of the average motor speed Ω.

$$\tilde{V} = K_a A \cos(\psi - \psi_c - \psi_K(\Omega)) \tag{5.3}$$

As similar low friction bearings have been implemented for the designed rotor from Chapter 4 Design, a control law similar to Equation (5.3) will be used.

5.3.1 Current controller

The current feedback loop in dq-frame implemented in the Moteus controller can be written as

$$\begin{aligned} u_q &= K_{P_i}(i_q^{ref} - i_q) + K_{I_i}\int (i_q^{ref} - i_q)\mathrm{d}t \\ u_d &= K_{P_i}(i_d^{ref} - i_d) + K_{I_i}\int (i_d^{ref} - i_d)\mathrm{d}t \end{aligned} \tag{5.4}$$

where K_{P_i} and K_{I_i} are constants for the current PI-controller.

5.3.2 Motor speed controller

The speed PI-controller implemented in the Moteus controller can be written as

$$\begin{aligned} i_q^{ref} &= K_{P_v}(\omega_{ref} - \omega) - K_{I_v}\int (\omega_{ref} - \omega)\mathrm{d}t + \frac{2}{3K_e}\tau_m^{ff} \\ i_d^{ref} &= 0 \end{aligned} \tag{5.5}$$

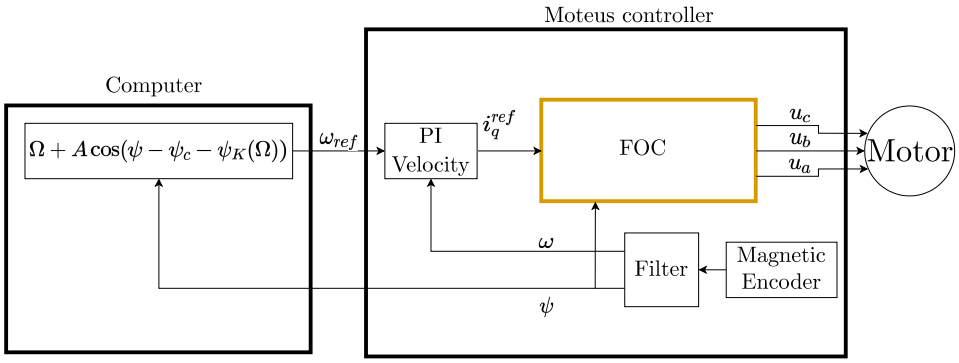

Figure 5.2: Harmonic motor speed feedback control.

where K_{P_v} and K_{I_v} are constants for the speed PI-controller and τ_m^{ff} is an optional torque feedforward. τ_m^{ff} is expressed in i_q by Equation (3.13). From the relation between motor torque and quadrature current in Equation (3.12), the resulting motor torque can be expressed.

$$\tau_m = \frac{3}{2} K_e \left[K_{P_v}(\omega^{ref} - \omega) + K_{I_v} \int (\omega^{ref} - \omega) \mathrm{d}t \right] \tag{5.6}$$

5.3.3 Harmonic motor speed control law

The principle of operation of the mechanism relies on a harmonic acceleration of the rotor. It is possible to formulate a sinusoidal motor speed feedback controller reference that results in sinusoidal rotor acceleration. The input reference to the speed controller is proposed as

$$\begin{aligned} \omega_{ref} &= \Omega + \tilde{\Omega} \\ \tilde{\Omega} &= A\cos(\psi - \psi_c - \psi_K(\Omega)) \end{aligned} \tag{5.7}$$

The motor speed reference can be inserted in the motor torque expression from Equation (5.6).

$$\tau_m = \frac{3}{2} K_e \left[K_{P_v}(\Omega - \omega) + K_{I_v} \int (\Omega - \omega) \mathrm{d}t + K_{P_v}(\tilde{\Omega}) + K_{I_v} \int (\tilde{\Omega}) \mathrm{d}t \right] \tag{5.8}$$

To compare this control law to the control law proposed by Paulos and Yim (2018), the constant motor torque at linearization point defined in Equation (2.19) is calculated. $\tilde{\Omega}$ is set to zero similar to how $\tilde{V}$ is set to zero in Equation (2.30).

$$\tau_{m_0} = -\frac{3}{2} K_e K_{i_v} \int (\omega - \Omega) \mathrm{d}t \tag{5.9}$$

The expression for τ_{m_0} in both Equation (2.30) Equation (5.9) is expected to be equivalent since both express the constant torque required for a constant speed. Equation (2.30) has two more terms than Equation (5.9). The current controller integral term hidden in

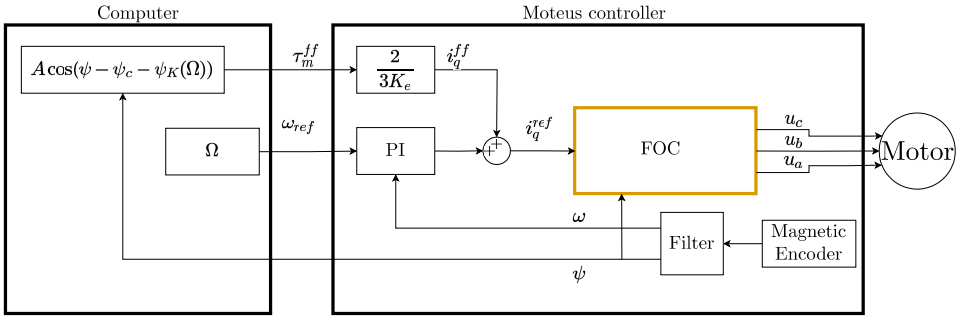

Figure 5.3: Torque feedforward control

Equation (5.9) should capture similar terms. The $3/2$ constant comes from the difference in motor modelling, Equation (2.30) uses a DC-motor model, Equation (5.9) uses a PMSM model. The $1/R_{ohm}$ constant appearing in Equation (2.30) comes from Equation (2.28) having voltage as output, while the speed controller has current defined as output. With these assumptions, the two expression are equivalent.

The perturbed motor torque $\tilde{\tau}_m = \tau_m - \tau_{m_0}$ is calculated similarly as in Equation (2.31).

$$\tilde{\tau}_m = -\frac{3}{2}K_e K_{P_v}\tilde{\omega} - \frac{3}{2}K_e K_{i_v}\tilde{\psi} + K_{P_v}\tilde{\Omega} + K_{I_v}\int(\tilde{\Omega})\mathrm{d}t \tag{5.10}$$

Compared to the structure of Equation (2.31), an additional integral term of the modulated signal $\tilde{\Omega}$ appears.

5.3.4 Harmonic torque feedforward

An alternative control law with harmonic motor torque modulation can enter through a torque feedforward term. The harmonic torque feedforward control law is proposed as

$$\begin{aligned} \omega_{ref} &= \Omega \\ \tau_m^{ff} &= A\cos(\psi - \psi_c - \psi_K(\Omega)) \end{aligned} \tag{5.11}$$

Similarly to Section 5.3.3, τ_m and $\tilde{\tau}_m$ can be calculated for this control law.

$$\tau_m = \frac{3}{2}K_e\left[K_{P_v}(\Omega - \omega) + K_{I_v}\int(\Omega - \omega)\mathrm{d}t\right] + \tau_m^{ff} \tag{5.12}$$

$$\tilde{\tau}_m = -\frac{3}{2}K_e K_{P_v}\tilde{\omega} - \frac{3}{2}K_e K_{i_v}\tilde{\psi} + \tau_m^{ff} \tag{5.13}$$

This expression has a similar structure to Equation (2.31). The integral term in terms of the modulated signal apparent in Equation (5.10) is not appearing with this feedforward modulation, as the speed PI controller is bypassed. In terms of the u_q voltage, an integral term will still appear due to the PI current controller. It is assumed that the electrical dynamics are much faster than the mechanical dynamics, such that the current controller can be tuned to a significantly higher bandwidth than the speed controller. This assumption also holds for the harmonic speed controller torque perturbations in Equation (5.10).

5.4 Tuning

5.4.1 Current controller

Tuning of the current controller is performed by pole placement. This is a part of the calibration script of the Moteus controller. A desired torque bandwidth is selected, this is used to set the bandwidth of the current controller. The poles are then placed based on the chosen bandwidth. The phase-locked loop filter for motor position is set by the driver to have twice the bandwidth of selected torque bandwidth. More filtering will result in smoother torque signal, while excessive filtering will limit torque bandwidth. Ideally, the mechanical dynamics of the motor should be evaluated to see what torque bandwidth is physically possible. The torque bandwidth was set to 200Hz after evaluating several bandwidths for dynamical performance versus vibrations.

5.4.2 Speed controller

A manual tune were performed for the speed controller. An initial tune were determined for the motor with no rotor attached. With the rotor mounted to the motor, higher gains were possible with the increased rotational inertia. A high gain were chosen, allowing a minimal amount of overshoot to maximize rise time.

5.5 Control implementation

To implement the proposed control laws, a Python 3 program were developed. The *moteus* python package were used to interact with the Moteus controller, and this package implements the CAN-FD communication. A *Motor* class were implemented, which can be initialized to use either the control law defined in Section 5.3.3 or the one in Section 5.3.3. A set of drive sequence routines with varying control input were developed to collect experimental data.

5.5.1 Soft startup routine

A problematic startup behaviour were identified. The unbalanced at rest behaviour described in Section 4.1.4 is problematic for sudden acceleration. A startup routine for the *Motor* class were implemented, limiting acceleration until a set minimum speed is achieved.

5.6 Experiment setup

The experimental test setup consists of the test rig from Section 4.2 and the rotor from Chapter 4 with motor controller as described in this chapter. Additional sensors such as an inertial measurement unit(IMU), a 6-axis force/torque sensor and a high speed camera is used. The force/torque sensor is used primarily to measure the thrust vector, while the IMU is used to look at vibrations. The IMU, force/torque sensor and motor driver is

Table 5.2: Control parameters used for experiments

Parameter	Value
K_{Pi}	0.0177 V/A
K_{Ii}	46.106 V/(As)
K_{Pv}	0.02 A/(rad/s)
K_{Iv}	0.01 A/rad
K_a	1
ψ_K	0

controlled from a computer. Figure 5.4 illustrates the IMU, force/torque sensor and rotor mounted on the test rig.

The IMU used is the VectorNav VN-100. Accelerometer and gyroscope data is sampled at 800Hz. The default sensor coordinate frame is used. Accelerations are measured in x, y, z axes as defined in Figure 5.4. Gyroscope yaw, pitch, roll angular rate measurements are defined as right-handed rotations around z, y, x respectively.

The 6-axis force/torque sensor used is the ATI Mini45. A data acquisition system reads analog strain gauge voltage measurements, and outputs processed values for force and torque in 6 axes. The system was configured to acquire analogue samples at 20kHz, averaging 10 samples and outputting 2kHz force/torque data to the computer. Further averaging with an exponential moving average method is performed on the computer. The reference frame for force/torque measurements were transformed from the sensors default to measure the thrust vector. This transformed frame is ground fixed at the center of the teetering hub, and consists of a translation of 74mm in positive z direction, and a negative 30 degree rotation about z. See Figure 5.4. The force/torque sensor has high uncertainty for the forces and torques that will be measured. The 95% confidence level measurement uncertainty for torques are in the order of magnitude of 0.1 Nm in the default coordinate system. For the transformed frame, this corresponds to 95% confidence level measurement uncertainty in the order of magnitude of 1N for x and y forces.

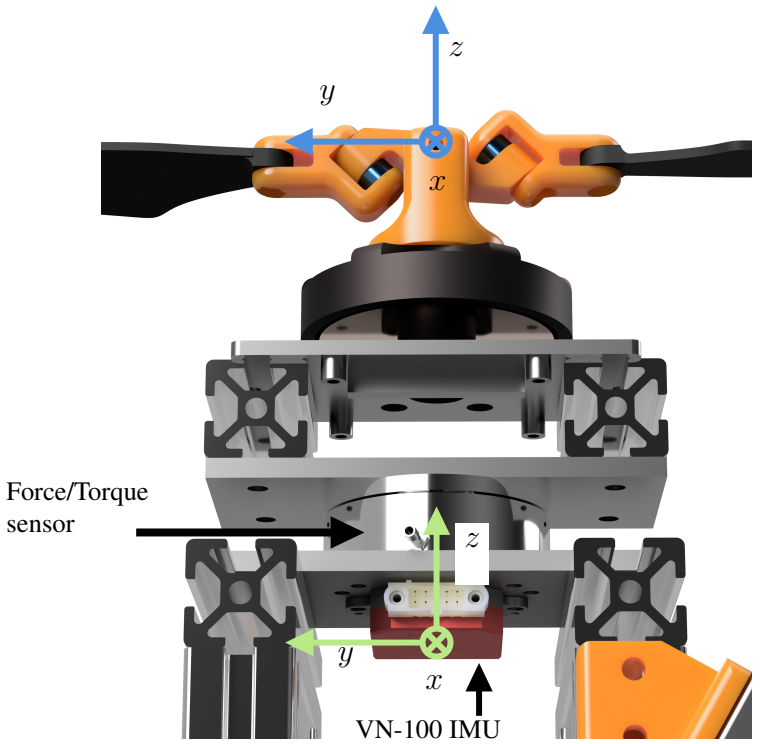

Figure 5.4: Measurement setup for rotor experiments. Force/torque sensor force axes are marked in blue. IMU acceleration axes are marked in green. Both frames are ground fixed and do not rotate with the rotor.

6

Experiment Results and Analysis

6.1 Testing scheme

The main goal of the experiments performed has been to evaluate thrust vector characteristics given the control laws proposed in Section 5.3. To limit the scope of evaluation, experiments are limited to the harmonic speed control law from Section 5.3.3. In evaluating thrust vector control against control law inputs, several different tests have been performed.

All data reported are collected with the rotor specified in Chapter 4 mounted to the motor. The coordinate frame for thrust vectoring is implemented as in Figure 1.6. This non rotating reference frame has the azimuth angle defined as right handed rotation about positive z. The zero azimuth angle is aligned with x. The zero elevation angle is defined parallel to the xy-plane. Relating this to the experimental test rig and sensor frames in Section 5.6 is simple, as the same x, y, z directions are used.

In all previous sections, a counter clockwise rotating rotor has been considered. The experimental data collected has been done for a clockwise rotating rotor. The only difference this presents is in relation to the direction of azimuth angle. In keeping the experimental presentation consistent, the thrust azimuth angle measurements has been mirrored to correspond to a counter clockwise rotating rotor.

When comparing data from high speed video frames and force sensor measurements, limitations apply. Video has only been captured for low motor speeds due to frame rate limitations. For the force sensor, the uncertainty is high as previously explained, and the most accurate data, with highest signal to noise ratio, will be for a large thrust vector magnitude. High speeds are therefore used for force sensor measurements.

6.2 Motor speed tracking

In achieving thrust vector control with the control law proposed, motor control is first evaluated. For the harmonic motor speed feedback controller, speed tracking within each

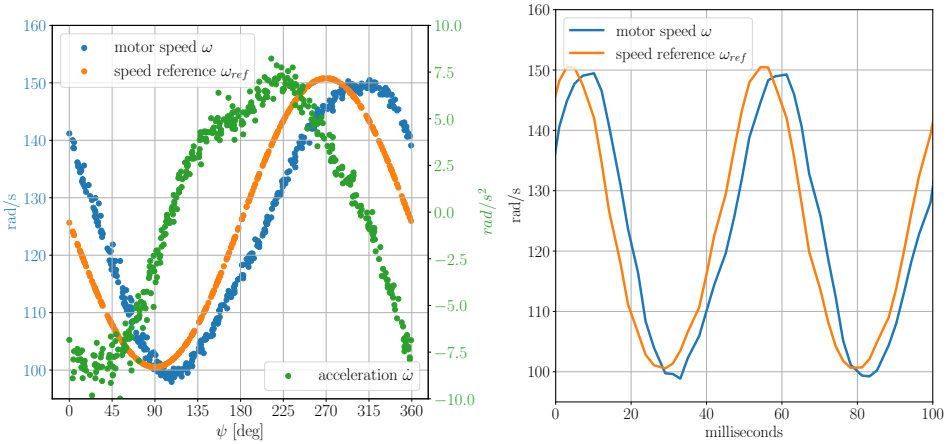

(a) Motor speed tracking vs motor position

(b) Motor speed tracking vs time

Figure 6.1: Motor speed tracking with harmonic speed controller. Average speed Ω is set to 20Hz. Motor speed modulation amplitude A is set to 0.2Ω. (a) shows collected motor speed and acceleration data over one second of operation.

revolution is an important performance metric. Speed tracking with the harmonic speed controller were measured for three different average motor speeds Ω, with harmonic modulation amplitude A set to 20% of Ω. An average speed of $\Omega = 20$Hz is shown in Figure 6.1, $\Omega = 40$Hz is shown in Figure 6.2 and $\Omega = 60$Hz is shown in Figure 6.3. The phase delay between speed reference and measured speed grows quite large with increasing motor speeds. For the $\Omega = 20$Hz response in Figure 6.1, the motor speed lags the reference by around 25°, or 4ms in terms of time. For the $\Omega = 60$Hz response in Figure 6.3, the motor speed lags the reference by around 70°, or 4ms in terms of time.

The python program developed to modulate harmonic control is not optimized for high bandwidth real time control. The average control rate achieved by this program were around 420Hz, commands are sent around every 2.5ms. The delay between a motor position measurement being taken, and the motor driver getting the updated command from the python program is therefore assumed to be around 2.5ms or potentially higher. Some of the phase lag in motor speed comes from these delays, apparent from the 4ms time lag in both the 20Hz an 60Hz response.

As for the amplitude response, a specific behaviour is noticed. The measured motor velocity is tracking the maximum motor speed setpoint well, while it overshoots the minimum speed reference. The effect is more prominent for the higher speeds. This is likely due to the aerodynamic drag, more specifically the Q-force as defined in Figure 2.1, causing torque acting as a dampener when the speed is increasing.

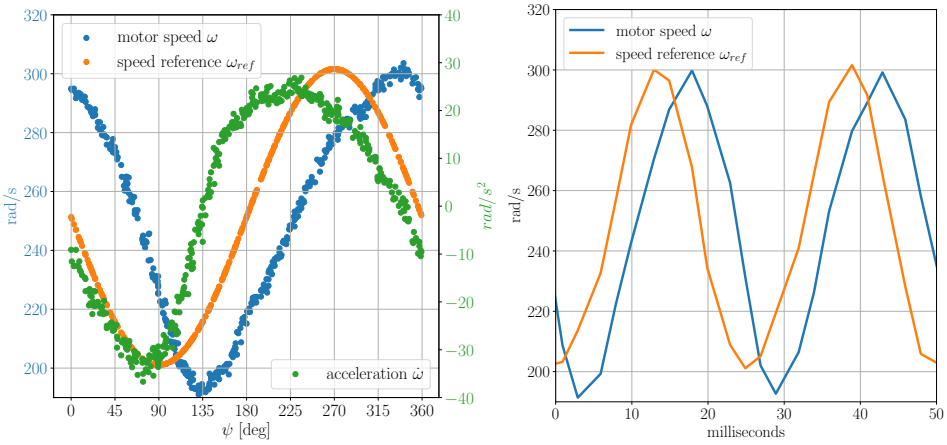

(a) Motor speed tracking vs motor position **(b)** Motor speed tracking vs time

Figure 6.2: Motor speed tracking with harmonic speed controller. Average motor speed Ω is set to 40Hz. Motor speed modulation amplitude A is set to 0.2Ω. (a) shows collected motor speed and acceleration data over one second of operation.

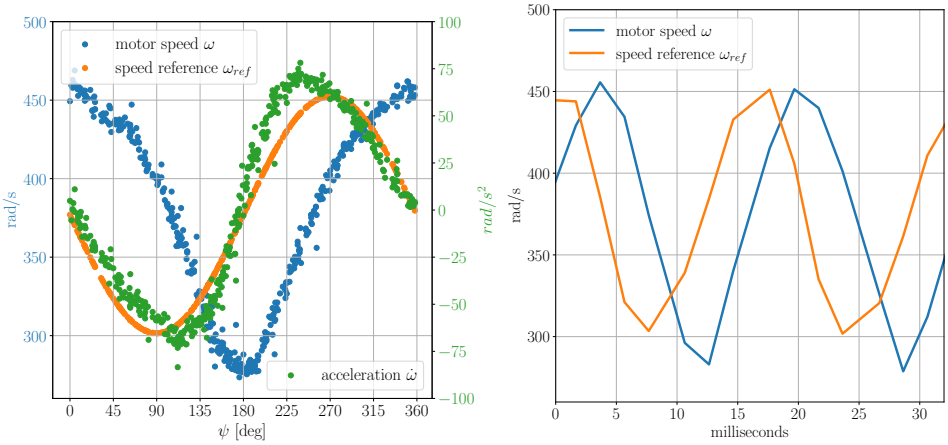

(a) Motor speed tracking vs motor position **(b)** Motor speed tracking vs time

Figure 6.3: Motor speed tracking with harmonic speed controller. Average motor speed Ω is set to 60Hz. Motor speed modulation amplitude A is set to 0.2Ω. (a) shows collected motor speed and acceleration data over one second of operation.

6.3 Rotor behaviour with harmonic modulation

Before evaluating thrust vector control, the behaviour of the rotor will be illustrated for clarity. Figure 6.4(b) shows image captures from high speed video during harmonic speed modulation. Motor position ψ is labeled at four positions spaced 90°apart in correspondence with the speed and acceleration in Figure 6.4(a). Label (3) motor position ψ corresponds to the azimuth angle ψ_c of the thrust vector.

From **Label (2)**, which shows the minimum teetering angle β, it can be seen in Figure 6.4(b) that the blades are lagging the motor position. In the corresponding motor position in Figure 6.4(a), the acceleration has crossed from negative to positive. This corresponds well with the lag behaviour. The kinematic coupling from lag to pitch will cause the blade pitch to increase for the positive blade, and decrease for the negative blade.

Label (3) shows the maximum teetering angle. The positive blade is raised, while the negative blade is lowered, as predicted from label (2). This position is seen to lag the maximum acceleration.

Label (4) shows the opposite behaviour as described for label (2). Acceleration has just crossed from positive to negative, and a blade lead effect is seen. This causes increased pitch for the negative blade, and decreased pitch for the positive blade.

In **Label (1)**, the maximum teetering angle is obtained, with the negative blade raised and the positive blade lowered. The acceleration is at the minimum.

There are some discrepancies between the acceleration and speed phase at the 180°offset positions. As an example, at label (3) the rotor position lags the maximum acceleration, but at label (1) there is little to no lag from the minimum acceleration. As the correspondence between the images and motor positions have been manually determined, the accuracy is too low to conclude where this discrepancy could come from.

6.4 Thrust vector evaluation

Two main experiments are performed with the harmonic speed control law. Figure 6.6 shows a sequence where average motor speed Ω is set constant, while the amplitude A is increased in steps. A is shown as a percentage of Ω.

Figure 6.7 shows an experiment where the average speed Ω is linearly increased, while A is kept as a fixed percentage of increasing Ω.

6.4.1 Thrust vector elevation

Thrust vector elevation β_c is proposed to be proportional to amplitude A in Equation (5.1).

Figure 6.5 shows thrust vector elevation versus harmonic amplitude for two different average speeds. The angles measured by the force sensor are the average of the ones appearing in Figure 6.6. The angles measured from video frames are shown in Figure 8.1. There is a clear linear trend in β_c against A, as previously shown by Qin et al. (2022) and Paulos et al. (2018).

In Figure 6.7, measured β_c, with A scaled by Ω, is appearing constant with Ω increasing. This indicates that scaling A by Ω directly without further calibration could be reasonable to achieve an approximate mapping to β_c for different speeds.

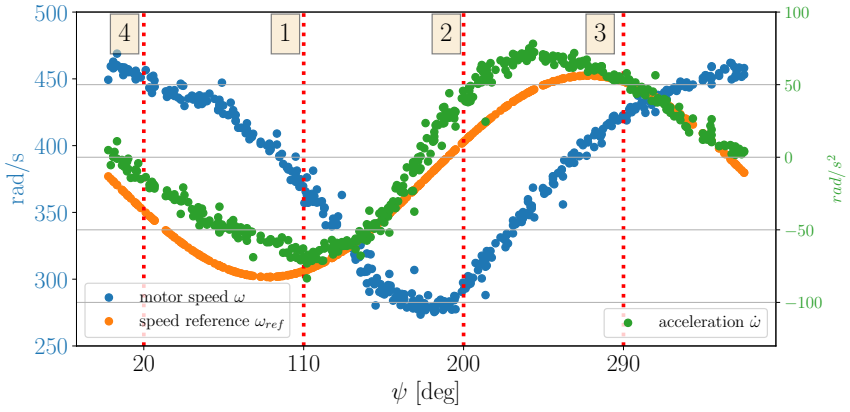

(a)

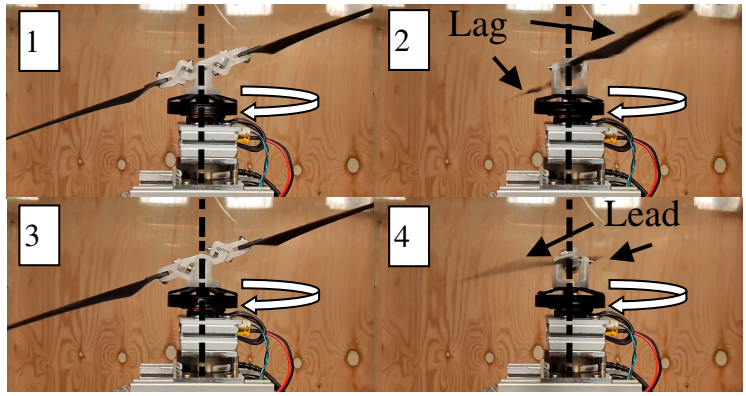

(b)

Figure 6.4: Single revolution harmonic speed modulated rotor behaviour. The numbered labels show approximately corresponding motor positions ψ between the graph (a) and images (b).

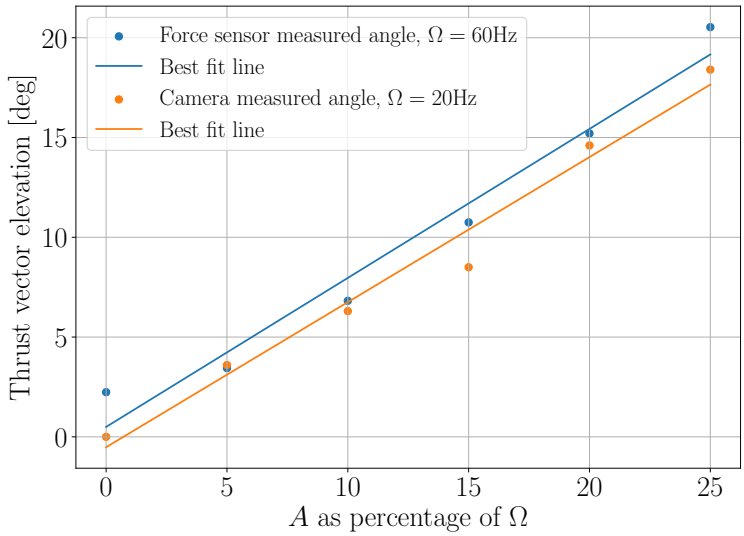

Figure 6.5: Thrust vector elevation angle against harmonic modulation amplitude A. Thrust sensor measurements as well as high speed video still frames from Figure 8.1 are used to determine the angle.

6.4.2 Thrust vector azimuth

Thrust vector azimuth angle ψ_c has been evaluated for a single angle offset, which was used to achieve a convenient direction for the experimental setup. The behaviour of interest in this case will be how ψ_c leads or lags the offset angle entering the sinusoidal term, and how it depends on the average motor speed and the control amplitude.

It is difficult to accurately determine ψ_c with the sensors used. Determining this angle with the force sensors relies on the relatively small, and low accuracy x and y forces. It is also difficult to measure with the camera setup.

From Figure 6.7 it can be seen that the thrust vector azimuth increasingly lags with increasing average motor speed. For lower speeds, ψ_c leads the offset angle in the sinusoidal modulator, while it lags increasingly with higher motor speeds. The thrust vector azimuth angle increases with around 50°from the 20Hz speed to the 60Hz speed. This lines up well to the phase lag observed in motor speed in Section 6.2.

The relationship between harmonic amplitude A and thrust vector azimuth angle ψ_c at average motor speed 60Hz can be seen in Figure 6.6. For higher amplitudes, the azimuth angle stays relatively unchanged with increasing amplitude. For lower amplitudes, the x and y forces are so small that the accuracy is not sufficient to give conclusions.

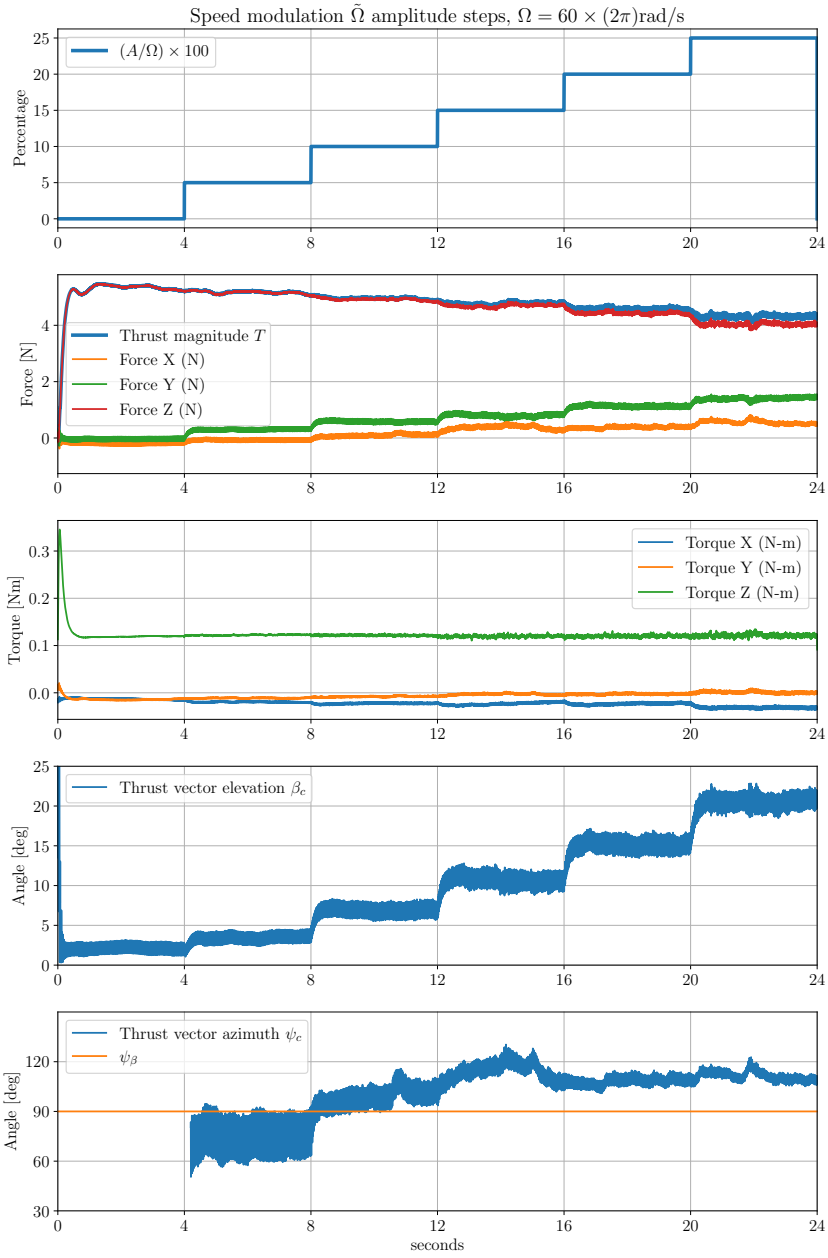

Figure 6.6: Experimental data with harmonic speed feedback controller. Average motor speed Ω is fixed to 60Hz. The $\tilde{\Omega}$ amplitude is increased in steps from 0 to 25% of Ω. Thrust vector angle is calculated from the force vector.

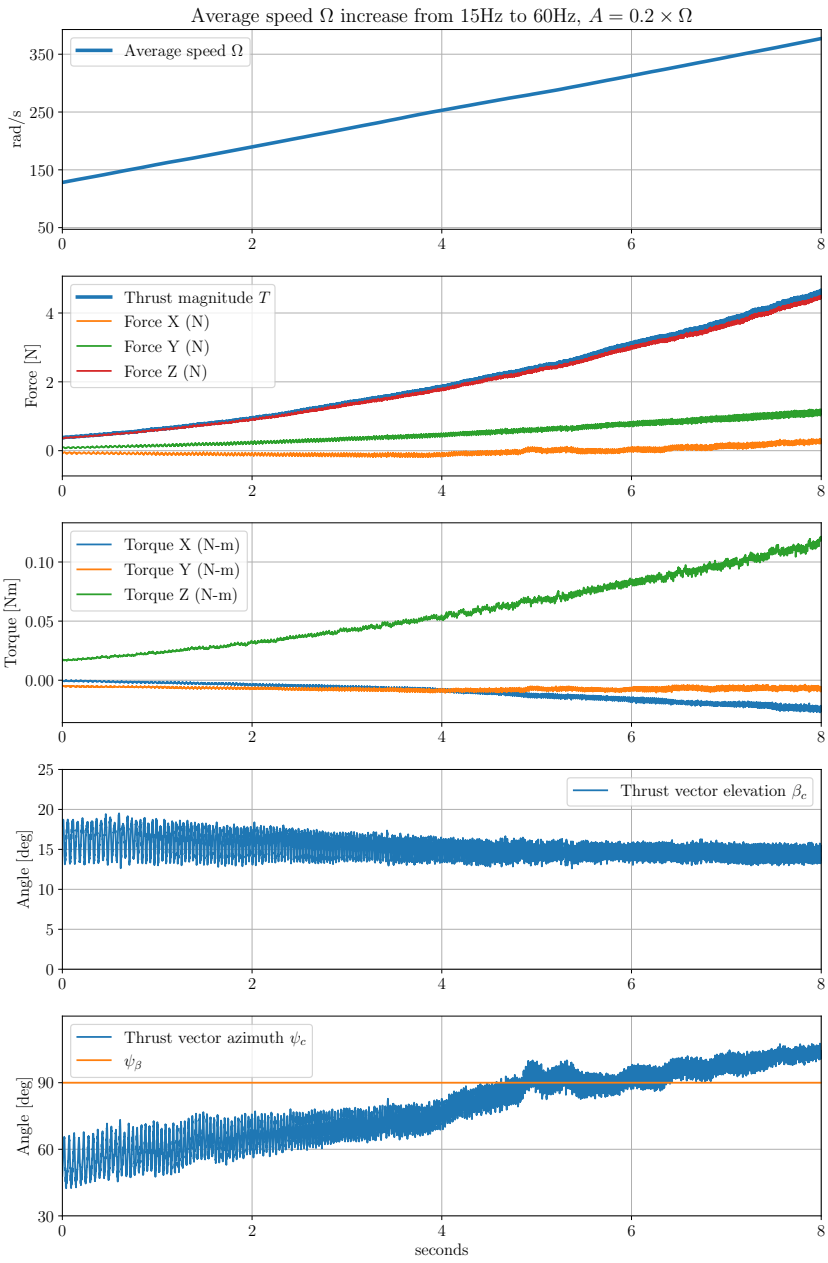

Figure 6.7: Experimental data with harmonic motor speed modulation. Average rotor speed Ω is increased from 15Hz to 60Hz. The $\tilde{\Omega}$ amplitude is set to 20% of Ω. Thrust vector angle is calculated from the force vector.

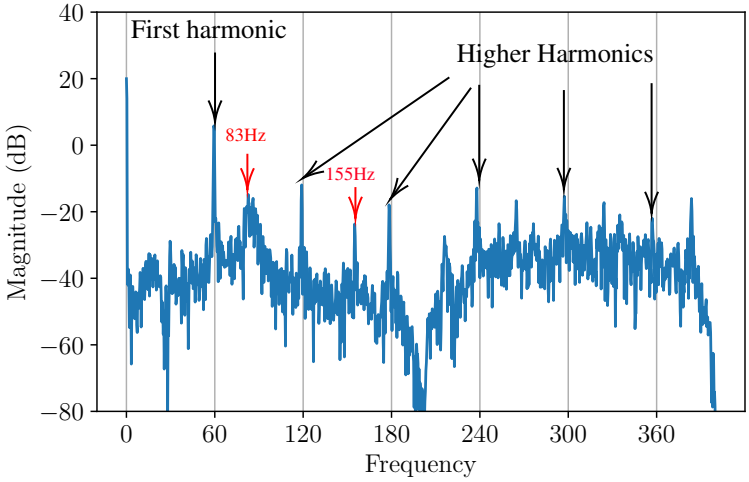

Figure 6.8: Magnitude spectrum of sum of x, y, z IMU acceleration. Rotor driven at average speed $\Omega = 60$Hz, harmonic amplitude $A = 0.2\Omega$

6.4.3 Thrust vector magnitude

For the thrust vector magnitude, it has been assumed that it will be a function of average motor speed Ω. What is most interesting in this case, is if the magnitude of thrust varies with harmonic drive amplitude A with a constant Ω. From Figure 6.6, the magnitude of thrust seems to decrease with increased elevation angle and amplitude A. It can also be noticed that there is a slight increase in torque about negative x-axis as the elevation angle increases. With the accuracy of the force measurements, it is difficult to conclude where the lowered thrust magnitude comes from. Alignment error between the reference frame used for forces and torques and the teetering hinge center could also cause apparent moments.

6.5 Vibrations

The frequency characterization of the system is important, especially for integration in an aerial vehicle. Vibration can cause unwanted noise for navigational systems. In the worst case, vibrations resonating with the airframe can cause catastrophic failure. Harmonic once-per-revolution excitation of teetering, lag and pitch is in this case exploited for control. A strong first harmonic frequency component is therefore expected, with higher harmonics of this frequency. For the linear model developed by Paulos and Yim (2018) this linear mode of the harmonic control is captured.

The magnitude spectrum of IMU accelerations has been evaluated for the rotor at harmonic amplitude $A = 0.2\Omega$, with average motor speed at 60Hz in Figure 6.8, and 40Hz in Figure 6.9. In both cases, there is a high first harmonic component. Higher harmonic components of the average motor frequency are also found. Frequency components of interest

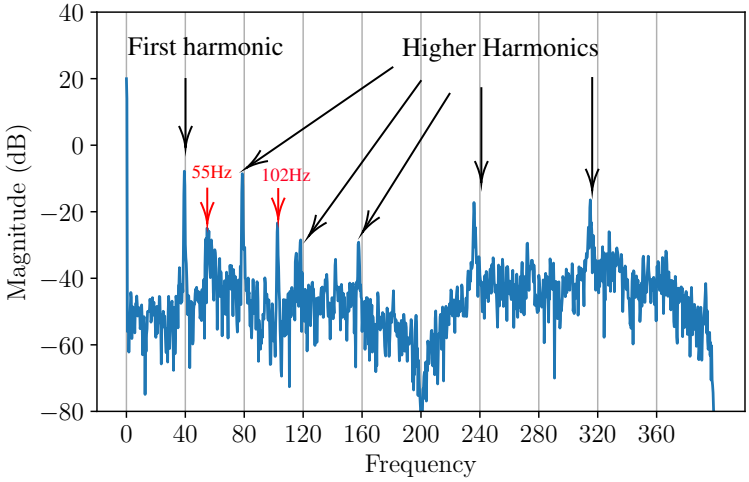

Figure 6.9: Magnitude spectrum of sum of x, y, z IMU acceleration. Rotor driven at average speed $\Omega = 40$Hz, harmonic amplitude $A = 0.2\Omega$

have been marked in red. In Figure 6.8, a component of frequency $83\text{Hz} = 1.38 \times 60\text{Hz}$ and a component of $155\text{Hz} \approx 2 \times 83\text{Hz}$ appears. For Figure 6.9 a component of frequency $55\text{Hz} = 1.38 \times 40\text{Hz}$ and a component of $155\text{Hz} \approx 2 \times 83\text{Hz}$. This frequency component appears at a factor of 1.38 of the average motor speed in both cases. This indicates that there is a non-linear mode of the rotor system large enough to appear.

Non motor speed dependent components are not easily found in these plots. These could come from the natural frequency of the structure, as well as accounting for the distance between the IMU and the rotor. The structure is likely stiff enough that the natural frequency is higher than what is captured here.

Qin et al. (2022) experienced problematic vibrations with higher sinusoidal amplitudes. This effect is demonstrated by the spectogram of x, y, z forces measured while increasing A in Figure 6.10. It is clear that the magnitude of most frequency components increase significantly as A is increased.

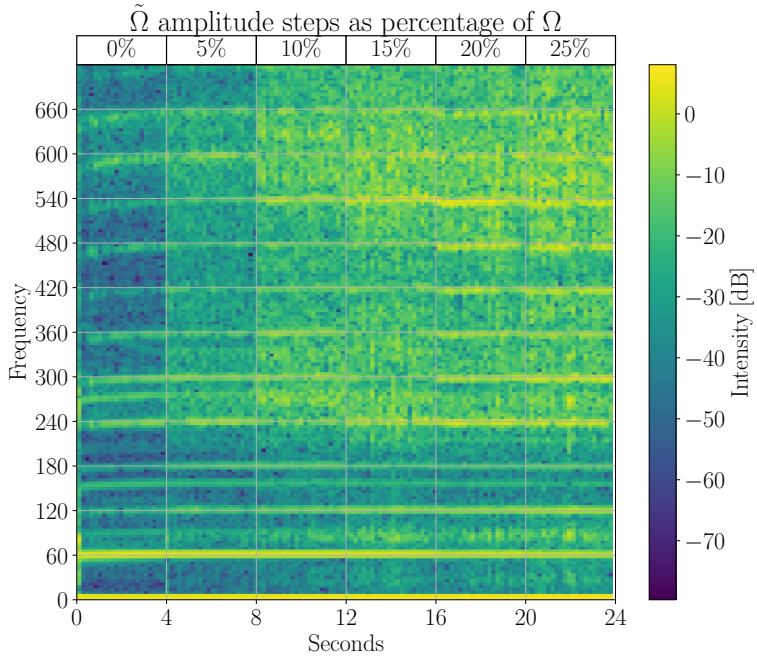

Figure 6.10: Spectogram of sum of x, y, z force at average motor speed $\Omega = 60$Hz while increasing harmonic modulation amplitude A.

7

Discussion

In controlling the thrust vector as described in Section 1.3, several necessary characteristics has been demonstrated. The requirement for thrust vector control is to find a the relation between a set of inputs to thrust vector elevation, azimuth and magnitude. For the harmonic velocity control law used, indication of such characteristics are demonstrated. The thrust vector elevation angle is shown to be approximately linear in terms of harmonic amplitude A applied. This agrees well with Qin et al. (2022) and Paulos et al. (2018), and a constant K_a can be found to map amplitude to elevation angle as in Equation (5.1). The characteristics of thrust vector azimuth angle also agrees with previous work from Qin et al. (2022) and Paulos et al. (2018). An average motor speed dependent lag offset from the harmonic modulation can be expressed as an azimuth angle $\psi_K(\Omega)$ in Equation (5.3).

While these relations suggests characteristics of the harmonically controlled rotor, final evaluation of specific thrust vector control is not shown. What would remain to control a desired thrust vector over a range of directions and magnitudes, is to perform a calibration for K_a, $\psi_K(\Omega)$ and $T(\Omega)$.

The motor control implementation with FOC has worked well for the used motor. As suggested in Section 3.6, this control scheme should offer some efficiency gains for the BLDCM used. For all tests performed, the motor temperature were checked by feel to see if excessive heat were generated. It was noticed that the motor never got noticeably warmer than room temperature after initial tuning. In comparison, Qin et al. (2022) notes that they limited A to 26% of voltage applied for their voltage modulation, partly due to the motor overheating. As experiments in this case limited A to 25% of average motor speed, further experiments at higher amplitude and higher average motor speed should be performed to evaluate performance gains. Additionally, steady operation is only considered here. Comparison between dynamical performance of the control techniques for BLDCM has not been considered.

Some comments can be made about the modulated sinusoidal signal in relation to the resulting motor speed trajectory in time. While the speed setpoint is sinusoidal in terms of motor position ψ, it is not sinusoidal in time. The parameter in the cosine term of the modulator, ψ is not linearly increasing with time, it depends on the motor speed ω, which

depends on ψ. As there is a once-per-revolution excitation, the motor will spend more time in the low speed part of the motor position compared to the high speed part. A smooth pulsing behaviour occurs, which becomes more prominent the higher the sinusoidal amplitude is as a percentage of average motor speed.

7.1 Further work

The data collected for analysis has been limited to experimental data. Evaluating experiments against the linear or the non-linear model would offer further insight.

Having more accurate force/torque measurements would allow better conclusions about thrust vector characteristics. Adding markers to track the hinges through high speed video would give valuable insight to hinge behaviour, which was done by Paulos and Yim (2018). By triggering the camera at a specific motor position, analysis such as the one in Section 6.3 could be performed much more precisely and conclusive.

As previously detailed, controlling the harmonic, motor position dependent control in the python program is not optimal, especially as motor drive frequency increases. An alternative, is to implement the harmonic controller in the Moteus FOC driver. It is open source, such that it would not be a monumental task to implement. The harmonic controller is simple compared to what is already running on the STM32G4 microprocessor at 30kHz, so performance should not be a problem. The computer would then only need to e.g. send reference input for A, Ω and β_c. Now the commands are invariant to rotor position, and can be can be sent at a much lower rate. This is somewhat analogous in concept to the benefits of controlling current in dq-frame. Data rate and delays from the communication protocol would be less of a challenge. Higher motor speed evaluation and vector control could be analyzed.

For the physical design of the rotor, it would be interesting to look at behaviour for a higher harmonic modulation amplitudes. That would require the design of the hubs to have greater clearance for hinge movements. The strength of the part is then important, and a stronger fabrication process than 3D-printing could be used.

8

Conclusion

A design and implementation of a rotor with kinematic coupling between lag and pitch has been developed. With an implementation of a harmonic speed modulation, characteristics of thrust vector control has been experimentally verified. Compared to previous work, a harmonic modulator in terms of mechanical rather than electrical output is implemented, and control modulation in terms of speed or torque with field oriented control is proposed. With a harmonic motor speed control law, the system has demonstrated necessary characteristics for control of the thrust vector. However, further calibration and evaluation is needed to fully control the desired thrust vector over a range of directions and magnitudes. The field oriented control algorithm used for motor control appears to offer efficiency gains for the brushless DC motor used, but further testing at higher amplitudes and average motor speeds is needed to fully evaluate its performance. The system that has been implemented shows great promise of integration in micro aerial vehicles with advantages in control, mechanical simplification and efficiency.

Bibliography

Bosso, A., Conficoni, C., Raggini, D., Tilli, A., 2021. A computational-effective field-oriented control strategy for accurate and efficient electric propulsion of unmanned aerial vehicles. IEEE/ASME Transactions on Mechatronics 26, 1501–1511. doi:10.1109/TMECH.2020.3022379.

Bousman, W., Center, A.R., Research, U.S.A.A., Activity, T., 1990. The Effects of Structural Flap-lag and Pitch-lag Coupling on Soft Inplane Hingeless Rotor Stability in Hover. AVSCOM technical report, National Aeronautics and Space Administration, Office of Management, Scientific and Technical Information Division.

Egeland, O., Gravdahl, J.T., 2002. Modeling and simulation for automatic control. Marine Cybernetics Trondheim, Norway.

Elaschke, F., Böhm, K., 1974. Verfahren der felderfassung bei der regelung stromrichtergespeister asynchronmaschinen. IFAC Proceedings Volumes 7, 635–649. doi:10.1016/S1474-6670(17)67912-6.

Flybotix, 2022. Flybotix Asio Drone. URL: https://flybotix.com/asio-drone/.

Gudmundsson, S., 2014. Chapter 9 - the anatomy of the wing, in: Gudmundsson, S. (Ed.), General Aviation Aircraft Design. Butterworth-Heinemann, Boston, pp. 299–399. doi:10.1016/B978-0-12-397308-5.00009-X.

Hasse, K., 1969. Zur dynamik drehzahlgeregelter antriebe mit stromrichtergespeisten asynchron-kurzschlusslaufer-maschinen. Dissertation TH. Darmstadt .

Leonhard, W., 2001. Control of Electrical Drives. Springer Berlin Heidelberg. doi:10.1007/978-3-642-56649-3.

Leutenegger, S., Hürzeler, C., Stowers, A.K., Alexis, K., Achtelik, M.W., Lentink, D., Oh, P.Y., Siegwart, R., 2016. Flying robots, in: Siciliano, B., Khatib, O. (Eds.), Springer Handbook of Robotics. Springer International Publishing. chapter 26. doi:10.1007/978-3-319-32552-1.

Li, Y., Qin, Y., Xu, W., Zhang, F., 2020. Modeling, identification, and control of non-minimum phase dynamics of bi-copter UAVs, in: 2020 IEEE/ASME International Conference on Advanced Intelligent Mechatronics (AIM), IEEE. doi:10.1109/aim43001.2020.9158910.

Ormiston, R.A., Hodges, D.H., 1972. Linear flap-lag dynamics of hingeless helicopter rotor blades in hover. Journal of the American Helicopter Society 17, 2–14. doi:10.4050/JAHS.17.2.2.

O'Rourke, C.J., Qasim, M.M., Overlin, M.R., Kirtley, J.L., 2019. A geometric interpretation of reference frames and transformations: dq0, clarke, and park. IEEE Transactions on Energy Conversion 34, 2070–2083. doi:10.1109/TEC.2019.2941175.

Paulos, J., Caraher, B., Yim, M., 2018. Emulating a fully actuated aerial vehicle using two actuators, in: 2018 IEEE International Conference on Robotics and Automation (ICRA), pp. 7011–7016. doi:10.1109/ICRA.2018.8462975.

Paulos, J., Yim, M., 2018. Cyclic blade pitch control without a swashplate for small helicopters. Journal of Guidance, Control, and Dynamics 41, 689–700. doi:10.2514/1.G002683.

Qin, Y., Chen, N., Cai, Y., Xu, W., Zhang, F., 2022. Gemini ii: Design, modeling, and control of a compact yet efficient servoless bi-copter. IEEE/ASME Transactions on Mechatronics , 1–12doi:10.1109/TMECH.2022.3153587.

Vertiq, 2022. Underactuated system. URL: https://www.vertiq.co/underactuated-system.

Appendix

A Camera still frames showing thrust vector elevation angle

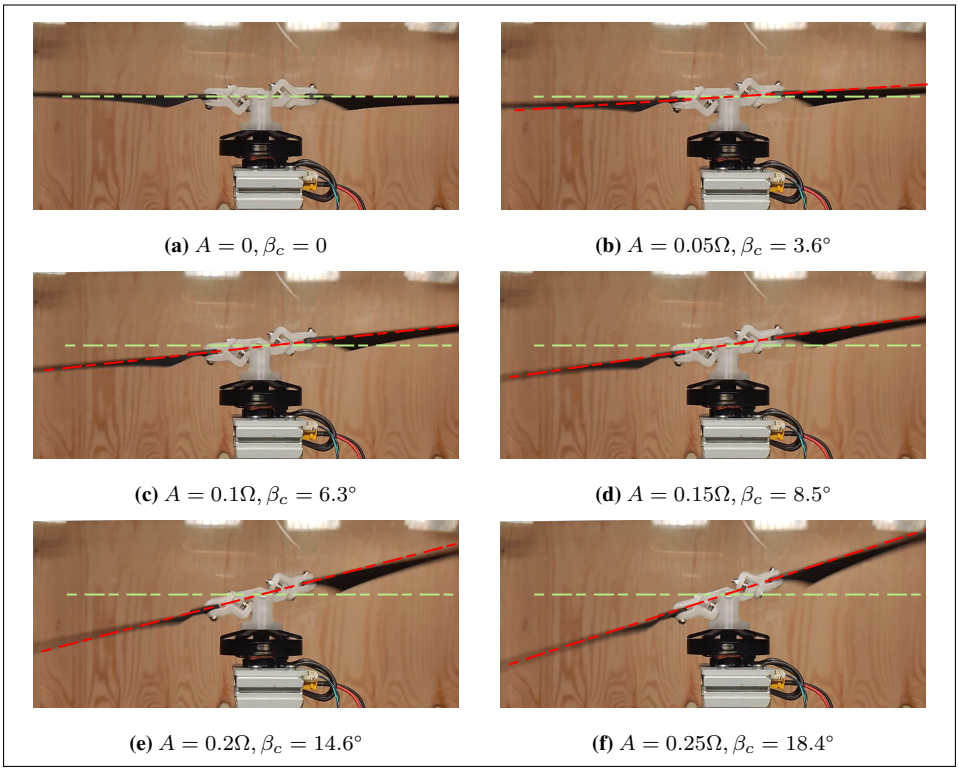

(a) $A = 0, \beta_c = 0$ **(b)** $A = 0.05\Omega, \beta_c = 3.6°$

(c) $A = 0.1\Omega, \beta_c = 6.3°$ **(d)** $A = 0.15\Omega, \beta_c = 8.5°$

(e) $A = 0.2\Omega, \beta_c = 14.6°$ **(f)** $A = 0.25\Omega, \beta_c = 18.4°$

Figure 8.1: Camera still frames with average motor speed $\Omega = 20$Hz with different harmonic modulation amplitudes A. Thrust vector elevation angle β_c is measured as the angle between the red and green line.